Homeostasis inside Single Activated Phagolysosomes: Quantitative and Selective Measurements of Submillisecond Dynamics of RoS/RNS Production with a Nanoelectrochemical Sensor

Yu-Ting Qi, Hong Jiang, Wen-Tao Wu, Fu-Li Zhang, Si-Yu Tian, Wen-Ting Fan, Yan-Ling Liu, Christian Amatore, Wei-Hua Huang

Homeostasis Inside Single Activated Phagolysosomes: Quantitative and Selective Measurements of sub-Millisecond Dynamics of ROS/RNS Production with a Nanoelectrochemical Sensor

Yu-Ting Qi,† Hong Jiang,† Wen-Tao Wu,† Fu-Li Zhang,† Si-Yu Tian,† Wen-Ting Fan,† Yan-Ling Liu,† Christian Amatore,*,‡,§and Wei-Hua Huang*,†

† College of Chemistry and Molecular Sciences, Wuhan University, Wuhan 430072, P. R. China

‡ State Key Laboratory of Physical Chemistry of Solid Surfaces, College of Chemistry and Chemical Engineering, Xiamen University, Xiamen 361005, P. R. China

§ PASTEUR, Département de Chimie, École Normale Supérieure, PSL Research University, Sorbonne University, UPMC Univ. Paris 06, CNRS 24 rue Lhomond, Paris 75005, France

KEYWORDS: phagolysosomes, homeostatic regulation, ROS/RNS differentiation, Pt NPs decorated nanowire electrode, nano bioanalytical electrochemistry.

ABSTRACT: Reactive oxygen and nitrogen species (ROS/RNS) are generated by macrophages inside their phagolysosomes. This production is essential for phagocytosis of damaged cells and pathogens, i.e., protecting our organism and maintaining immune homeostasis. The ability to quantitatively and individually monitor the four primary ROS/RNS ($ONOO^-$, H_2O_2, NO, and NO_2^-) with sub-millisecond resolution is clearly warranted to elucidate the still unclear mechanisms of their rapid generation and to track their concentrations variations over time inside phagolysosomes, in particular, to document the origin of ROS/RNS homeostasis during phagocytosis. A novel nanowire electrode (NWE) has been specifically developed for this purpose. It consisted of wrapping a SiC NW with a mat of 3 nm platinum nanoparticles (Pt NPs) whose high electrocatalytic performances allow the characterization and individual measurements of each of the four primary ROS/RNS. This allowed for the first time a quantitative, selective and statistically robust determination of the individual amounts of ROS/RNS present in single dormant phagolysosomes. Additionally, the sub-millisecond resolution of the nanosensor allowed confirmation and measurement of the rapid ability of phagolysosomes to differentially mobilize their enzyme pools of NADPH oxidases (NOX) and inducible nitric oxide synthases (iNOS) to finely regulate their homeostasis. This reveals an essential key to immune responses and immunotherapies and rationalizes its biomolecular origin.

INTRODUCTION

Macrophages play a significant role in immune protection by eliminating pathogens, cellular debris, necrotic and damaged cells. When encountering pathogens, macrophages activate and stretch pseudopodia to grab and internalize pathogens into their cytoplasm by encapsulating them inside vacuoles called phagosomes. These then combine with lysosomes, another type of vacuole equipped with active enzymes bound to their membranes, to generate phagolysosomes.[1-6] To efficiently digest their endocytic contents while avoiding cellular self-damage, these enzyme pools include NADPH oxidases (NOX) and inducible nitric oxide synthases (iNOS) that are supposed to be activated to produce fluxes of superoxide ions ($O_2^{\cdot-}$) and nitric oxide (NO). These two parent species undergo follow-on reactions that give rise to a cocktail of four primary reactive oxygen (ROS) and nitrogen (RNS) species (e.g., $ONOO^-$, H_2O_2, and NO_2^-) that shred pathogens down to molecular levels.[7-10]

Studies published over the past decades have provided significant understanding of the generation, regulation, and roles of ROS/RNS in resistance to infection, based on the analysis of endpoints or long-term consequences (from minute to week).[11,12] This suggested, although it could only be established recently by two different strategies,[13,14] that once intra-phagolysosome ROS/RNS are depleted, NOX and iNOS rapidly (within milliseconds) replenish $O_2^{\cdot-}$ and NO to maintain the high phagolysosome performance. However, the kinetic regulation of the enzymes' activities and the precise nature of the mechanisms that maintain ROS/RNS content in phagolysosomes at levels high enough to digest unwanted biological material without endangering macrophages still remain undetermined.[9,10,12-14] We wish to show here that a new, specifically designed class of platinized SiC nanowire electrodes (SiC@Pt NWEs) provides substantial answers to these important questions related to ROS/RNS-based immunoprotection by enabling statistically significant dynamic measurements of four

Scheme 1. Schematic diagrams describing the fabrication of SiC@Pt NWEs for quantitative differentiation of ROS/RNS in individual phagolysosomes. A) Two-step electroless plating of SiC@Pt NWs. B) Mounting a SiC@Pt NW at the tip of a nanopipette for intracellular differential measurement of four primary ROS/RNS ($ONOO^-$, H_2O_2, NO, NO_2^-) at four different electrochemical potentials.

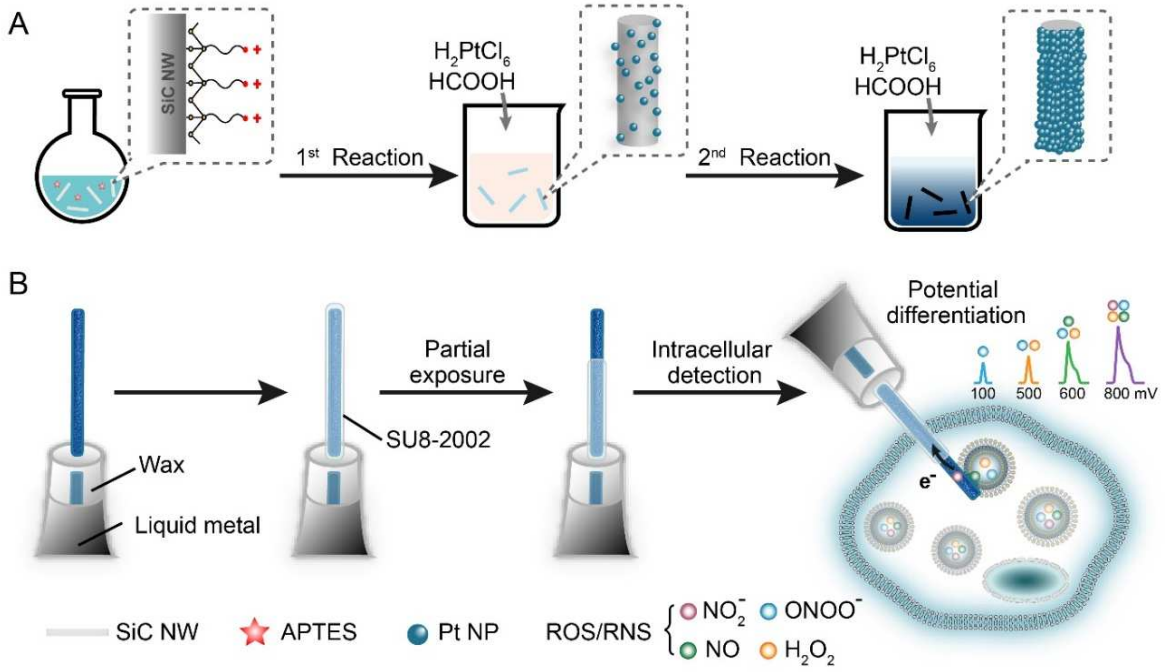

primary ROS/RNS ($ONOO^-$, H_2O_2, NO, NO_2^-) production at the single phagolysosome level inside living activated macrophages.

RESULTS AND DISCUSSION

Principle of the Present Experimental Strategy. Cylindrical nanoelectrodes of nanometer diameter allow to penetrate through the membranes of living cells and organelles while keeping their integrity and their functionalities to carry out sensitive electroanalytical measurements in their interior with selectivity and spatio-temporal resolution to characterize and quantify the internal dynamics of molecular species at the single cell level or organelle level.[10-21] This is possible because the high aspect ratio of these electrodes allows them to impose a strong localized pressure against the cell membrane so that a tight nanopore opens[22] through which the nanoelectrode can slip while the membrane immediately seals back around it. This makes it possible to maintain unchanged the mechanisms ensuring intracellular metabolism during the progression of the electrode inside the cellular cytoplasm.

Ensuring and maintaining the nanosensors' ability to detect and differentiate oxidation waves of the four primary ROS/RNS ($ONOO^-$, H_2O_2, NO, NO_2^-) while preventing any degradation of their responses require the nanosensor to be coated with platinum black (Pt-black).[10,20,23-27] For example, nanopipette-based electrodes fitted with embedded Pt-black deposits encased at their tips and functioning as scanning electrochemical microscopy (SECM) probes could be inserted into single phagolysosomes to individually monitor and quantify during tens of minutes the four primary ROS/RNS with quadruple potential chronoamperometric sequences. This pioneered direct measurements of long-term dynamic changes in ROS/RNS inside large, intact phagolysosomes as they underwent a homeostatic activity.[13] However, to avoid corrupting the faradic information with residual charging currents due to large areas of platinum black, the method had to have a time resolution of a few seconds at best. Moreover, the difficulty of its SECM operation did not allow monitoring a sufficient number of events during a reasonable time duration to draw statistically significant conclusions.[12,13] For this reason, we developed in parallel another strategy based on platinized carbon deposited SiC nanowire electrodes to analyze ROS/RNS effluxes released by individual phagolysosomes with a temporal resolution down to milliseconds in order to study the processes of establishment of homeostasis at short times.[14,17] However, the quasi-crystalline Pt coatings of these nanoelectrodes did not provide sufficient electrochemical resolution to differentiate the four primary ROS/RNS, so only their overall quantity and dynamics could be determined.[12] Thus, a new strategy capable of measuring ROS/RNS inside single living cells and their intracellular organelles with sufficient spatial, kinetic and chemical resolution is clearly needed in order to better monitor and reveal the physiological homeostatic processes taking place inside the phagolysosomes of macrophages while gathering a sufficient collection of data to offer important statistical information.

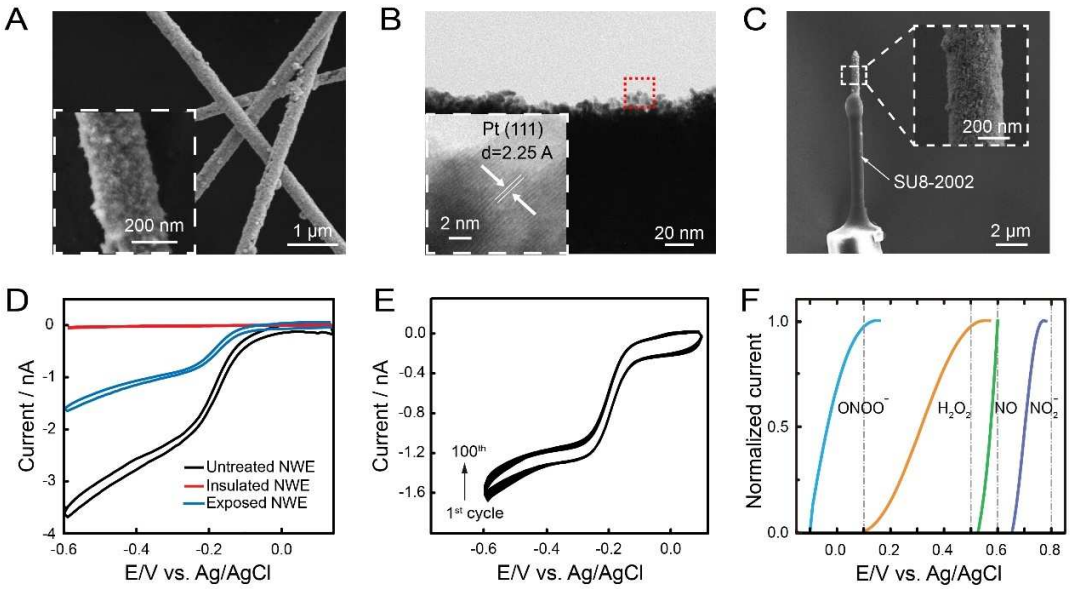

Figure 1. A) SEM images of SiC@Pt NWs; inset: enlarged SEM image showing details of the SiC@Pt NWs. B) TEM image of the edge of a SiC@Pt NW; inset: HRTEM of Pt NPs located in the red rectangle in main view. C) SEM of a SiC@Pt NWE; inset: a magnified SEM image of its exposed part (*ca.* 160 nm radius) at the tip of the insulated section. D) CVs of 1 mM $Ru(NH_3)_6^{3+}$/1 M KCl at an untreated, insulated and tip-exposed SiC@Pt NWE confirming the decrease of the Ru(III) reduction current by 98% and 60%, respectively (n = 5) as expected based on its SEM geometry in C. E) Repetitive CVs (100 cycles) of 1 mM $Ru(NH_3)_6^{3+}$ /1 M KCl of an exposed SiC@Pt NWE. F) Voltammetric oxidation of $ONOO^-$ (blue curve, 1 mM, pH=10.0), H_2O_2 (orange curve, 1 mM, pH=7.4), NO (green curve, 1 mM, pH=7.4) and NO_2^- (purple curve, 1 mM, pH=7.4) in PBS solution; currents were normalized to their maximum value to help comparison. Vertical dashed lines indicate the optimal detection potentials for each ROS/RNS species (see text).

Based on the two previous attempts described above, it was concluded that the key issue to achieve this objective resided in a perfect design of the nanostructure of the Pt deposit to ensure the sought electrocatalytic properties. This problem was solved by constructing a high-density coating of contiguous ultrasmall Pt nanoparticles (Pt NPs) using their spontaneous electrostatic grafting onto the previously modified surface of bare SiC nanowires (SiC NW) by positive 3-aminoprooyltriethoxysilane (APTES) monolayer (Scheme 1A). Due to the excellent electrical conductivity of the dense coating of nanoscale Pt NPs bonded by electrostatic interactions on the surface of APTES-modified SiC and their high electrocatalytic properties, the SiC@Pt nanowire electrodes (NWEs) made it possible to discriminate and monitor individually the four primary ROS/RNS ($ONOO^-$, H_2O_2, NO, NO_2^-) and measure their dynamic fluxes with sub-millisecond temporal resolution when combined with the IVIEC (intracellular vesicle impact electrochemical cytometry) technique introduced by Ewing et al[28-30] (Scheme 1B).

SiC@Pt NWEs could then be appropriately inserted into single macrophages and monitored therein for the dynamic concentrations of each of the four primary ROS/RNS released by a series of phagolysosomes with the required sensitivity, precision and selectivity with a sub-millisecond temporal resolution. As will be developed in what follows, these measurements highlighted that when the concentrations of ROS/RNS inside a phagolysosome decrease below a threshold value due to their electrooxidation at the SiC@Pt NWE tip, mimicking what happens when they react with biological moieties, iNOS and NOX are immediately activated to compensate for ROS/RNS losses. This is quite consistent with the homeostatic behavior observed before.[12-14] However and unexpectedly, iNOS and NOX responses were found to be extremely different on sub-millisecond timescales. iNOS greatly increased their activity to release large amounts of NO, while NOX could only generate relatively weaker fluxes of $O_2^{\cdot-}$ at the beginning.[31,32] On larger timescales, $O_2^{\cdot-}$ began to be continuously generated by the NO-regulated NOX pool,[33] eventually producing a dynamic ROS/RNS homeostatic response essentially composed of $ONOO^-$ and NO excess, whose composition differs radically from those inside resting phagolysosomes, thereby providing unsuspected new insights into the key mechanisms supporting phagocytosis.

Fabrication and Characterization of Single SiC@Pt NWEs. As summarized in the previous section, Pt NPs were successfully grafted on SiC NWs surfaces by a simple chemical reduction method (Scheme 1) after the SiC NWs surfaces were modified with 3-aminoprooyltriethoxysilane (APTES) to make the surface uniformly positively charged for promoting the absorption of the negatively charged chloroplatinic anion ($PtCl_6^{2-}$) (Figure S1).[34,35] $PtCl_6^{2-}$ was then reduced by formic acid (HCOOH) to form Pt nanonuclei (Pt NNs) with the size and morphology suitable for optimal electrocatalytic performance.[36-40] Once the Pt nucleation started, a large number of Pt NNs spontane-ously formed onto the surface of SiC NWs (Figure S2). However, pursuing the reaction beyond this stage triggered an autocatalytic reduction of $PtCl_6^{2-}$ onto the Pt NNs surface, yielding too large Pt aggregates (Figure S3).[41,42] Such large Pt aggregates presented a too low detection sensitivity and

most of all exhibited a poor chemical resolution among the four primary ROS/RNS as occurred in our previous works.[17,43] To avoid forming such large aggregates, the Pt NNs-modified SiC NWs were ultrasonically re-dispersed in the reaction solution to re-uniformize the Pt nucleation in order to ultimately coat the SiC nanowire surface with a high density of ultrasmall Pt NPs (ca. 3nm in diameter) forming a Pt layer about 50 nm thick (Figure 1A and Figure S4). High-resolution TEM indicated that the resulting Pt NPs had a mean diameter of *ca.* 3 nm and a lattice spacing of 0.225 nm corresponding to (111) planes (Figure 1B).[38,39] SEM-EDX mapping and XPS confirmed the successful and reproducible fabrication of batches of SiC@Pt NWs (Figure S5 and Figure S6).

The ensuing nanoelectrochemical sensors were assembled by inserting individual SiC@Pt NWs into a pulled glass micropipette filled with liquid metal and wax while leaving a length of *ca.* 10 µm protruding out of the sealed micropipette (Figure 1C).[17,44] To ensure that no extracellular signals could be detected after inserting sealed SiC@Pt NWEs inside cells, their whole surfaces were first entirely insulated with a thin SU8-2002 photoresist layer. Dipping the tip of these mounted SiC@Pt NWEs in acetone dissolved the photoresist and exposed a *ca.* 300 nm diameter Pt-modified electroactive tip with a length of *ca.* 2-3 µm (Figure 1C, Scheme 1B, Figure S7, and Figure S8). The consistency of the fabrication procedure was assessed by recording steady-state cyclic voltammograms (CVs) for the reduction of 1 mM $Ru(NH_3)_6^{3+}$ (i) after mounting them, (ii) after their complete insulation, and (iii) after exposing their tip (Figure 1D). The excellent stability of the insulation and of the electroactive Pt tip was confirmed by monitoring the resilience of CV Ru(III) reduction currents for hundreds of CV cycles (compare Figure 1E). The reproducibility of the sizes and electrocatalytic performance of the final SiC@Pt NWEs was excellent, even though the SiC@Pt NWs were fabricated in large batch batches. For example, compare the excellent reproducibility (standard deviation of 3.2%) of H_2O_2 oxidation CV currents obtained with eight SiC@Pt NWEs mounted with eight randomly selected SiC@Pt NWs in Figure S9.

Electrocatalytic Performance of SiC@Pt NWEs *vs.* the Four Primary ROS/RNS. The voltammetric oxidations of each of the four key ROS/RNS ($ONOO^-$, H_2O_2, NO, NO_2^-) were recorded independently at these SiC@Pt NWEs (Figure S10) to provide a reference set of normalized oxidation voltammograms at physiological pH 7.4 (Figure 1F) except for $ONOO^-$ whose calibration solutions needed to be prepared at pH 10.0 due to its life time of a few seconds at most except under alkaline conditions.[24] As observed, the oxidation currents of $ONOO^-$ and H_2O_2, on the one hand, and of H_2O_2 and NO, on the other hand, overlapped slightly (<5% for normalized currents) while that of NO_2^- was well separated from the others. Note that the electrocatalytic properties of Pt NPs formed on the SiC@Pt NWEs in this work differed from those of the Pt-black tips used in previous works by some of us.[11-13,23-26] Accordingly, the oxidation potentials order determined for $ONOO^-$ and H_2O_2 resulted inverted but this was irrelevant to the performance and application of the current nanosensors. Optimal detection potentials (+100, 500, 600, 800 mV *vs.* Ag/AgCl) shown by the vertical dashed lines in Figure 1F should have been selected in order to differentiate each primary ROS/RNS while minimizing interference from other ROS/RNS.[11-13,23-26] However, successfully applying the IVIEC method to phagolysosomes required that NWEs potential was set at 500 mV at least.[28-30] Below this value, most of the phagolysosomes hitting the nanosensor tip did not release their content. Accordingly, all the oxidation of all four primary ROS/RNS species could be amperometrically recorded, but those of $ONOO^-$ and H_2O_2 could not be monitored individually since their oxidations occurred simultaneously at 500 mV (see below for their individual resolution).

Charges of amperometric spikes recorded during ROS/RNS releasing events (see later) reflect more adequately the fluxes of ROS/RNS released by application of Faraday law.[25, 26] Charges are additive for all species oxidizable at each of the above potentials, resulting in the following system of linear equations:

$$Q_{800\ mV}=Q_{ONOO^-}+Q_{H_2O_2}+Q_{NO}+Q_{NO_2^-} \quad (1)$$

$$Q_{600\ mV}=Q_{ONOO^-}+Q_{H_2O_2}+Q_{NO} \quad (2)$$

$$Q_{500\ mV}=Q_{ONOO^-}+0.95Q_{H_2O_2} \quad (3)$$

where $Q_{species}$ is the charge featuring the complete oxidation of the released species, while $Q_{potential}$ is the total charge measured at one given potential.[25,26] The charge values corresponding to the complete oxidation of each ROS/RNS released quantities could thus be simply deduced through solving the above linear system of equations.

IVIEC measurements are performed by fast amperometry, so we controlled that the recorded currents were not altered over the time scales considered by investigating the relationship between the voltammetric peak currents (i_p) and scan rate (v) monitored for H_2O_2, NO and NO_2^- at the present SiC@Pt NWEs. This showed that the oxidations of these species are diffusion-controlled (i_p values being proportional to $v^{1/2}$), and similar CV shapes were recorded over the range of scan rates (Figure S11). These two results demonstrated that the selectivity represented by equations (1-3) remained valid whatever the time spans of the recorded spikes.

Quantitative Differentiation of ROS/RNS in Individual Phagolysosome. RAW 264.7 murine macrophages were pretreated during 24 h with interferon-γ (IFN-γ) and lipopolysaccharide (LPS) to mimic an in vivo inflammatory situation.[45-48] Bight-field microscopy images confirmed the successful transformation of macrophages from their resting type (M0) into their activated one (M1) as evidenced by significantly larger size and drastic shape changes (Figure 2Aa-b). [49,50]

SiC@Pt NWEs could be easily moved across the membrane of M0 or M1 RAW 264.7 macrophages resting in PBS containing the inert $Ru(NH_3)_6^{3+}$ cation whose charge prevented its penetration inside the cell cytoplasm. The progressive disappearance of the Ru(III) reduction current (Figure 2Ac-d and Figure 2B) was then directly reporting on the gradual penetration of SiC@Pt NWEs through the cell membrane. When it was pulled out of the cell, the $Ru(NH_3)_6^{3+}$ reduction current was almost restored to its

value initially measured outside the cell (*ca.* 90% in Figure 2B) demonstrating that the SiC@Pt NWE sensing tip was not significantly altered during its penetration and its performance inside macrophages. Importantly, NEW-penetrated M1 cells maintained their high viability during and after SiC@Pt NWEs insertion as checked by fluorescent staining with Calcein-AM and propidium iodide (PI) (Figure 2C).

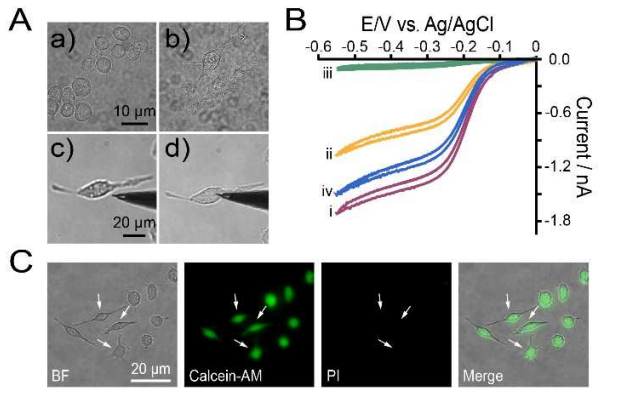

Figure 2. A) Bright-field images of (a) M0 and (b) M1 (stimulated with IFN-γ/LPS for 24 h) RAW 264.7; view of a SiC@Pt NWE (c) before and (d) after complete insertion into a M1 type macrophage. B) CVs recorded at different penetration depths of one SiC@Pt NWE within a M1 type RAW 264.7 placed in a 1 mM $Ru(NH_3)_6^{3+}$ PBS bath: (i) before insertion, (ii) after *ca.* 50% insertion of the electroactive tip, (iii) after its complete insertion, and (iv) after its withdrawal out of the cell. C) Bright-field (BF) and fluorescent microscopy images of M1 type RAW 264.7 cells inserted by SiC@Pt NWEs (indicated by arrows) after staining with Calcein-AM and propidium iodide (PI) as indicated (the "merge" view is composed by the merging of bright-field, Calcein-AM and PI fluorescent images).

Importantly, no current spikes could be observed upon using NWEs fabricated by depositing a carbon layer and no Pt NPs to monitor M1 cell types (Figure S12). This excluded any possible interference from other electroactive substances. In M1 cell types, many ROS/RNS-loaded phagolysosomes hit sequentially the electroactive tip during each single insertion experiment so that an amperometric trace consisting in a sequence of spikes (Figure 3Aa-c) was generated at each of the three potentials identified above (+500, 600, 800 mV *vs.* Ag/AgCl) featuring a succession of successful IVIEC events during which all phagolysosomes hitting the nanosensor tip opened and released their content.[28-30]

In order to distinguish H_2O_2 and $ONOO^-$, M1 type RAW 264.7 cells were preincubated with a specific scavenger of H_2O_2 (catalase-polyethylene glycol, CAT)[51] or of $ONOO^-$ (5, 10, 15, 20-tetrakis (4-sulfonatophenyl) porphyrinato iron (III) chloride, FeTPPS)[52-54]. The products (H_2O, O_2, NO_2^-, NO_3^-) of these two scavengers could not be detected at the potential +500 mV, thus could not cause interference in the measurements. No current spikes were observed at +500 mV when the cells were preincubated with both scavengers (CAT and FeTPPS), illustrating the effectiveness of each scavenger (Figure S13A). After the cells were treated with FeTPPS to scavenge $ONOO^-$, the resulting spikes were too small to obtain reliable statistics since their maximum currents were less than only 1-2 pA while the current noise had generally a *ca.* 5 pA peak-to-peak amplitude (Figure S13B). On the contrary, when the cells were incubated with CAT to scavenge H_2O_2 (the inhibition effect was also confirmed by fluorescent staining by DCFH-DA, Figure S14), a series of amperometric spikes displaying substantial current were recorded at +500 mV (Figure 3Ad). Altogether, these inhibitors-based experiments demonstrated that H_2O_2, if any, was present at extremely low concentrations in the phagolysosomes, so that $ONOO^-$ could be detected alone at +500 mV. The two other ROS/RNS were detected at +600 mV (NO + $ONOO^-$) and +800 mV (NO_2^- + NO + $ONOO^-$) (Figure 1F), and their individual oxidation charges were deduced by application of the set of linear equations (1-3) (Figure 3Aa-b).

Statistical analyses revealed that charges Q, i.e., the i-t spikes areas, obeyed log-normal distributions (Figure 3B) with maxima and half-widths values exhibiting significant differences depending on the applied potential: $\log_{10}Q_{800\ mV}$=-13.7±0.28 , $\log_{10}Q_{600\ mV}$=-13.9±0.15 , $\log_{10}Q_{500\ mV}$=-14.2±0.20 , and $\log_{10}Q_{500\ mV+CAT}$=-14.4±0.16 (Figure 3C). The average quantities of each primary ROS/RNS, $n_{ROS/RNS}$, in zeptomoles per phagolysosome could then be calculated according to equations (1-3) and Faraday's law, Q=nzF where F = 96 500C is the Faraday constant and z is the electron stoichiometry of the species electrochemical oxidation ($z_{H_2O_2}=z_{NO_2^-}=2$, $z_{ONOO^-}=z_{NO}=1$).[11] $n_{H_2O_2}$=10 zmol , n_{ONOO^-}=45 zmol, $n_{NO_2^-}$=45 zmol, and n_{NO}=80 zmol were thus obtained (Figure 3D).

Importantly, almost no spikes could be recorded (Figure S15) after adding specific inhibitors of NOX (apocynin) and iNOS (NG-monomethyl-L-arginine monoacetate salt or 1400W dihydrochloride) to the IFN-γ/LPS culture medium of RAW 264.7. This confirmed the crucial roles of iNOS and NOX membrane-bound phagolysosomes enzymes in the production of $O_2^{\cdot-}$ and NO that acted as precursors of all released ROS/RNS.[11] Their initial quantities of these two parent species produced in an average phagolysosome could be evaluated according to the stoichiometries in Figure S16,[11] as summarized in Figure 3D: $n_{O_2^{\cdot-}}^{parent}$=110 zmol and n_{NO}^{parent}=170 zmol.

The initial production of the parent superoxide ions is *ca.* only half of the parent NO in agreement with a previous report by some of us.[13] In addition, it is noted that the radical-radical coupling between NO and $O_2^{\cdot-}$ occurs at the diffusion limit, i.e., $k_{coupling}$ = (4−16) × 10^9 M^{-1} s^{-1}, while the disproportionation of $O_2^{\cdot-}$ is slower even in the presence of SOD, i.e., k_{disp} = (1−2) × 10^9 M^{-1} s^{-1}, and is certainly much less rapid in the absence of SOD as expected inside phagolysosomes.[11,55,56] Hence, most of the superoxide ions have to end up under the form of peroxynitrite and then of nitrite ion its follow up product (Figure 3D), leaving out about 50% of unreacted NO *vs.* its initial production. The

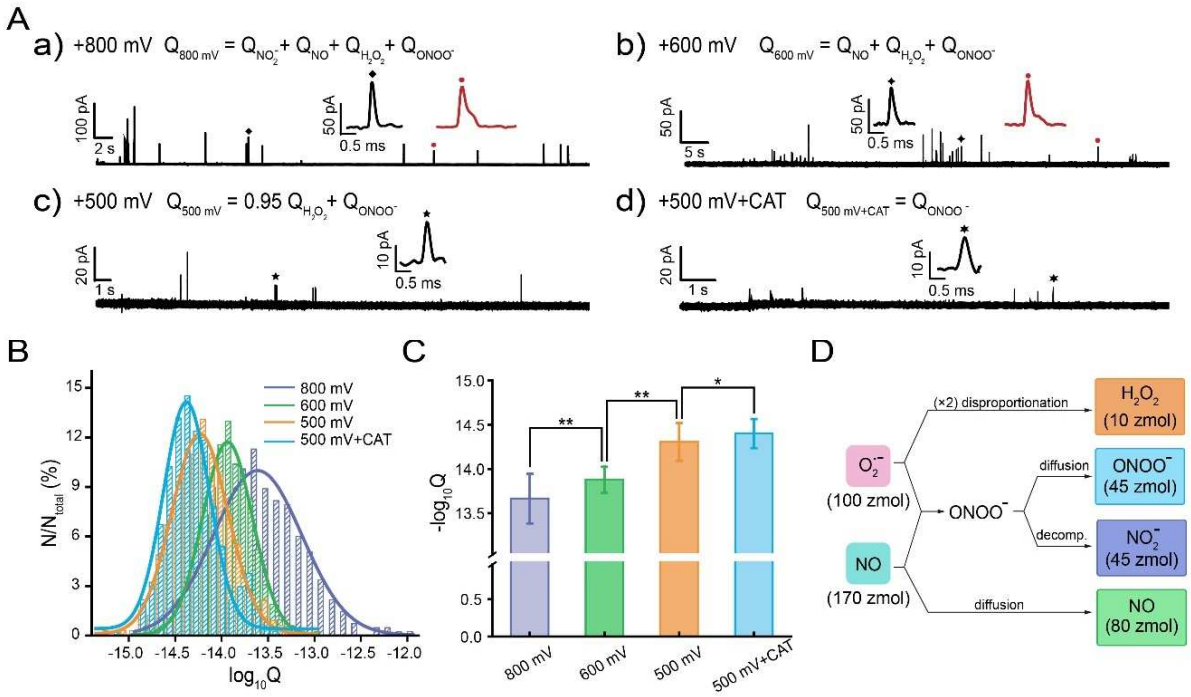

Figure 3. A) Representative amperometric traces recorded after insertion of SiC@Pt NWEs into IFN-γ/LPS stimulated RAW 264.7 macrophages at (a) +800 mV, (b) +600 mV, (c) +500 mV and (d) +500 mV+CAT (see text). Typical events marked with an asterisk in each trace are shown at large resolution (the red asterisks indicated spikes with shoulders, while black ones indicated normal IVIEC spikes). B) Normalized log-normal histograms ($\log_{10}Q$) describing the frequency distributions of the charge values detected at different potentials (purple, +800 mV, n=416 events from 20 cells; green, +600 mV, n=425 events from 17 cells; orange, +500 mV, n=403 events from 15 cells; blue, +500 mV+CAT, n=418 events from 20 cells). C) Statistical analyses of the $\log_{10}Q$ at different potentials (means ± SEM; one-way ANOVA, **p ≤ 0.01， *p ≤ 0.05). D) Scheme of the chemical relationships between four primary ROS/RNS and their precursors $O_2^{\cdot-}$ and NO. The average amounts of substance (n) of each species are indicated in parentheses.

presence of this important residual excess of NO in activated M1 cells was also confirmed by the high fluorescent intensity observed upon staining the cells with the NO probe DAF-FM DA (Figure S17), while staining with DCFH-DA (ROS probe) gave rise to a much lower fluorescent intensity (Figure S18).

Data Analysis of Spikes with Shoulders. In a previous work by some of us in which all primary ROS/RNS were detected at +850 mV,[14] it was noticed that a majority 0f spikes displayed "shoulder" (see inset in Figure 4B), i.e., currents falloff tails that significantly deviated from the normal exponential expected behavior. This evidenced the existence of a fast ROS/RNS homeostasis, indicating that the activities of NOX and iNOS enzymes were either reactivated or boosted to swiftly produce fresh ROS/RNS within milliseconds in order to maintain a highly scavenging activity inside phagolysosomes even though their initial ROS/RNS load was removed by its oxidation at the nanoelectrode tip surface. In full agreement with this previous work, a large variety of spikes monitored in this work displayed similar "shoulders". Interestingly, the percentage of spikes displaying such a typical feature was lower at lower potentials: from 75% of the events at +800 mV, to only 65% at +600 mV and less than 10% at +500 mV (with or without pretreatment with CAT) (Figure 4A). Such a low percentage at +500 mV indicated that H_2O_2 and $ONOO^-$ did not significantly contribute (i.e., less than 10%) to this homeostatic issue. A similar conclusion is drawn about NO_2^- since its maximum fraction is again around 10% at most (viz. equal to the difference between 75% and 65%). This implies that NO is the main species produced during these homeostatic events, thus suggesting that only iNOS are efficiently triggered during homeostatic processes at short times.

In order to further investigate this issue, the spikes exhibiting shoulders were analyzed based on a previously established kinetic model (see Equation (1) in reference (14)) that allows separating the contributions of diffusional release of (i) the initial quantity, Q_0 (green area in the inset in Figure 4B) of ROS/RNS stored inside a phagolysosome before it undergoes an IVIEC event,[28-30] from (ii) that, Q_{prod} (orange area in the inset in Figure 4B), produced after the fast consumption of the initial content is drastically decreased during IVIEC events triggered a homeostatic production of fresh ROS/RNS. Briefly, the method amounts to deconvolute mathematically the current time variations, $i_0(t)$, featuring the release flux due to the stored material based on the behavior of the spike current, i(t), before the inflexion point located on its descending trend.[57] Extrapolating mathematically the current-time function $i_0(t)$ beyond this point and

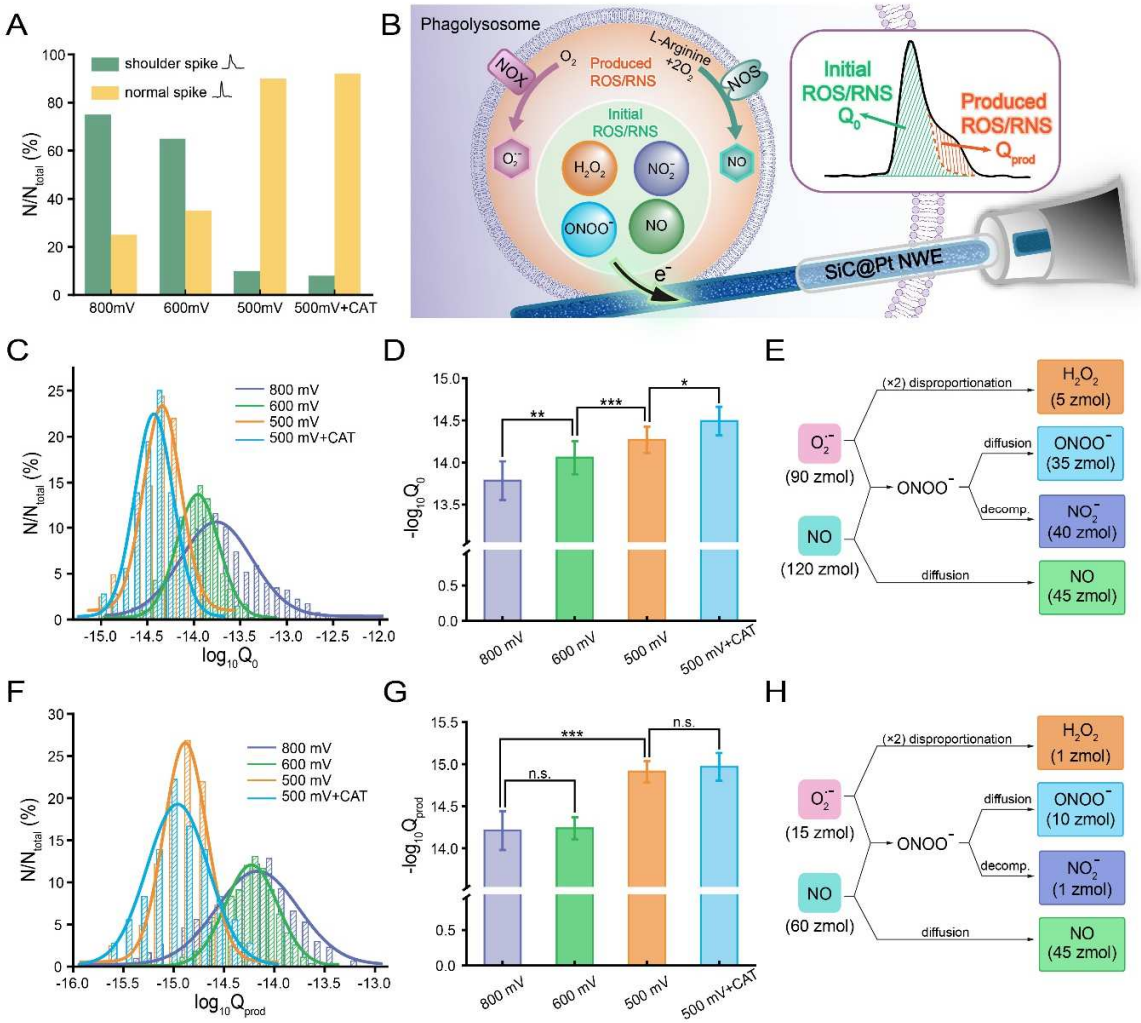

Figure 4. A) Proportions of normal peaks and peaks with distinctive shoulders recorded as a function of the detection potentials. B) Principle of quantitative monitoring of initial and freshly produced ROS/RNS released by individual phagolysosomes with a single SiC@Pt NWE during one IVIEC event. C,F) Normalized histograms describing the frequency of log-normal distributions of the initial charges Q_0 (C) and freshly produced charges Q_{prod} (F) of detected ROS/RNS at different potentials (purple, +800 mV, n=316 events from 20 cells; green, +600 mV, n=279 events from 17 cells; orange, +500 mV, n=43 events from 7 cells; blue, +500 mV+CAT, n=35 events from 10 cells). D,G) Statistical analyses of the logarithm of initial charges Q_0 (D) and freshly produced charges Q_{prod} (G) of ROS/RNS detected at different potentials (means ± SEM; one-way ANOVA, ***p ⩽ 0.001, **p ⩽ 0.01, *p ⩽ 0.05, n.s.: not significant). E,H) Recapitulative schemes of the chemical relationships between the four primary detected ROS/RNS and their precursors $O_2^{\cdot-}$ and NO observed in M1 RAW 264.7 macrophages based on the initial phagolysosome contents (E) or on the freshly produced ones (H); the quantities, n, of each species are shown in parentheses.

subtracting it from the total current provides the current $i_{prod}(t)$ featuring the release of the freshly produced ROS/RNS through quick homeostasis.[14] Q_0 and Q_{prod} are then readily obtained by independent time integrations of $i_0(t)$ and $i_{prod}(t)$ respectively.

Statistical analyses revealed that both Q_0 (Figure 4C) and Q_{prod} (Figure 4F) obeyed log-normal distributions. The statistical results of Q_0 values measured at different potentials were significantly different: $\log_{10}Q_{0,\,800\,mV}$=-13.8±0.23, $\log_{10}Q_{0,\,600\,mV}$=-14.1±0.20, $\log_{10}Q_{0,\,500\,mV}$=-14.3±0.12, and $\log_{10}Q_{0,\,500\,mV+CAT}$=-14.5±0.16 (Figure 4D). This corresponds to the cocktail of ROS/RNS shown in Figure 4E, i.e., $n^0_{H_2O_2}$=5 zmol, $n^0_{ONOO^-}$=35 zmol, n^0_{NO}=40 zmol, and $n^0_{NO_2^-}$=45 zmol which stem from the initial synthesis of $n^{parent,0}_{O_2^{\cdot-}}$=90 zmol and $n^{parent,0}_{NO}$=120 zmol. Note that these values are less than those derived from the global analysis of all spikes, i.e., including both the main spikes (Q_0) and the shoulders (Q_{prod}) when they exist.

These results establish that H_2O_2 only accounts for 5% of the initial content of phagolysosomes before they undergo an IVIEC occurrence, in conformity with the function of phagolysosomes of eliminating pathogens, impaired cells and organic debris.[45] This is in full agreement with the fact that the protonated form ONOOH (pKa = 6.8) of peroxynitrite acts as an extremely efficient molecular scissor by spontaneously generating OH radicals in lipidic environments,[58-61] while H_2O_2 requires the presence of free transition metal ions to do the same.

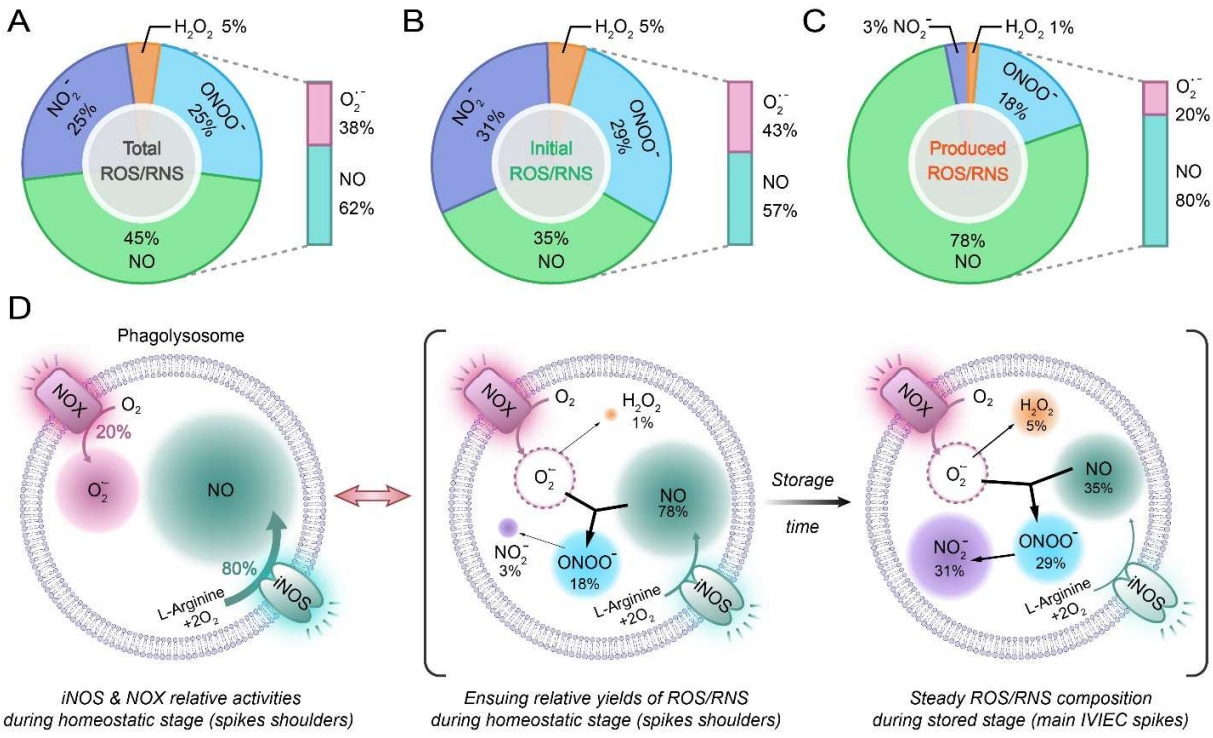

Figure 5. Relative proportions of the four primary ROS/RNS (H_2O_2, $ONOO^-$, NO and NO_2^-) and of their two precursors ($O_2^{\cdot-}$ and NO) within (A) global content (stored + homeostatic), (B) stored quantities (normal "IVIEC components" of current spikes), and (C) freshly produced during the homeostatic phase ("shoulder components"). D) Graphical summary of possible mechanisms coherent with the detected ROS/RNS quantities (relative diameters of color patches associated to the four primary ROS/RNS represent their relative detected quantities; thicknesses of arrows represent the relative kinetic magnitudes of the reactions occurring within phagolysosomes).

Contrastingly, Q_{prod} values recorded at +800 mV ($\log_{10}Q_{prod,\ 800\ mV}$=-14.2±0.23) and +600 mV ($\log_{10}Q_{prod,\ 600\ mV}$=-14.2±0.13) presented no significant difference confirming that the homeostatic events giving rise to the spikes' shoulders generated mostly NO as already remarked above. Accordingly, released quantities monitored at +500 mV ($\log_{10}Q_{prod,\ 500\ mV}$=-14.9±0.12) or +500 mV after pretreatment with CAT ($\log_{10}Q_{prod,\ 500\ mV+CAT}$=-15.0±0.17) were identical and comparatively smaller, evidencing a small production of peroxynitrite ions and almost none of hydrogen peroxide during the homeostatic response at short times (Figure 4G). The average values of the corresponding quantities of ROS/RNS (Figure 4H) were indeed: $n^{prod}_{H_2O_2}$=1 zmol , $n^{prod}_{ONOO^-}$=10 zmol, n^{prod}_{NO}=45 zmol, and $n^{prod}_{NO_2^-}$=1 zmol. These quantities allowed to evaluate those of the $O_2^{\cdot-}$ and NO precursors generated to produce the homeostatic response: $n^{parent,prod}_{O_2^{\cdot-}}$=15 zmol and $n^{parent,prod}_{NO}$=60 zmol. This confirmed that iNOS are responsible of *ca.* 80% of the homeostatic response, essentially yielding NO, while NOX that usually form $O_2^{\cdot-}$ corresponded to *ca.* only one fifth of it. These figures compare drastically with the almost equivalent productions of $O_2^{\cdot-}$ and NO that were responsible for the amount of ROS/RNS stored in phagolysosomes of activated M1 RAW 264.7 macrophages.

Figure 5A-C summarizes these findings and compares the average proportions of each of the four primary ROS/RNS (H_2O_2, $ONOO^-$, NO and NO_2^-) as well as those of their corresponding precursors, $O_2^{\cdot-}$ and NO, that were detected globally (Figure 5A), i.e., without distinguishing between those that were initially stored inside the phagolysosomes (Figure 5B), or produced during the homeostatic response to an IVIEC episode (Figure 5C). Interestingly, in contradiction with the general belief that digestion of unwanted biological material in phagolysosomes of activated macrophages was mostly ensured by Fenton reactions involving a specific production of H_2O_2, it is observed that hydrogen peroxide is the ROS/RNS with the lowest proportion, either in stored contents (<5%) or in those produced during homeostatic episodes (<1%). Considering that NO_2^- is a decay end-product of peroxynitrite ions, it is also observed that the global production of $ONOO^-$,[55,56] as represented by the sum of $ONOO^-$ and NO_2^- quantities, is the essential species stored within phagolysosomes (*ca.* 60%, Figure 5B).

This proportion drops in the homoeostatic response (*ca.* 20%, Figure 5C) mostly because NO is then the major parent precursor (*ca.* 80%) *vs.* $O_2^{\cdot-}$ (*ca.* 20%) (Figure 5C). This may be due to the short time duration elapsed between the production and the detection of NO (milliseconds at most), so in contrast with the longer time durations experienced during the storage phases, it may not have time to diffuse away. Indeed, NO may easily diffuse across bilipidic membranes such as those of phagolysosomes.[58,60] Note that the

importance of the time duration in our experiments is also evidenced by the extremely small ratio of NO_2^- *vs.* $ONOO^-$ in the released homeostatic pulses (*ca.* 15% at most of initial $ONOO^-$ could decay into NO_2^-, Figure 5C) compared to the larger ratio for stored material (*ca.* 50% of initial $ONOO^-$ had decayed into NO_2^-, Figure 5B). Such interpretation is perfectly coherent with the sequential cartoons shown in Figure 5D.

NOX and iNOS Enzymes Activities during Storage *vs.* Homeostatic Responses. The above results evidenced that the relative proportions of each primary ROS/RNS significantly differed depending on whether their stored contents (i.e., oxidized in the main IVIEC current spike component) or their homeostatic responses (i.e., the spike shoulders) were considered. To our knowledge, this is a previously unsuspected information of considerable importance for understanding the behavior of the most fundamental players in our immune system. Indeed, up to know it was implicitly thought that the two stages involved in the same way of phagolysosomes' NOX and iNOS pools. At present, we cannot offer a definitive answer as to why this is happening, but do offer a hypothetical rationalization for this startling finding nonetheless.

It must first be remembered that the activity of NOX enzymes in phagocytes is necessarily transient because the assembled NOX can retain their active structure for at most a few minutes before disassembling.[31, 32] Therefore, the actual production of $O_2^{\cdot-}$ is time-dependent, being finely controlled by the dynamic balance between the assembly and disassembly processes of transmembrane NOX. Conversely, iNOS enzymes can generate large amounts of NO by acting over prolonged periods (several hours to several days) after being assembled in response to pathogenic stimulation.[32] Yet, importantly, NO in turn regulates the activity of NOX enzymes through concentration changes to minimize collateral damage from ROS species.[32] Based on these two known facts, a new perspective can be offered on the process of rapid ROS/RNS production in relation to short-term homeostatic responses (Figure 5D).

Once the ROS/RNS are significantly consumed by reacting with biological materials captured inside a phagolysosome (a situation mimicked in our work by the oxidation of ROS/RNS on the surface of the SiC@Pt during IVIEC events), the still reactive iNOS enzymes may perform to renew intravesicular NO content. In contrast, partially assembled NOX enzymes may produce only small amounts of $O_2^{\cdot-}$ which immediately reacts in less than a millisecond with local excess NO to form $ONOO^-$ and not produce any amounts of H_2O_2. This transient behavior corresponds to the "shoulder currents" monitored by SiC@Pt NWEs through oxidation of the limited cocktail described in Figure 5C. On the other hand, when phagolysosomes have matured over long periods, continuous production of $O_2^{\cdot-}$ by NO-regulated NOX activity may result in higher yields of H_2O_2 and $ONOO^-$. Simultaneously, the intra-phagolysosome concentration of NO can also decrease significantly due to its easy diffusion across the membrane of the phagolysosome,[10,60] while over long storage times, $ONOO^-$ can significantly decompose to NO_2^-, its stable end product (Figure 5B).[55, 56] The steady state amounts of ROS/RNS resulting from these dynamics inside phagolysosomes (compare the kinetics in Figure 5D, right-hand side cartoon) give rise to the normal IVIEC component of current spikes.

CONCLUSIONS

A new and robust electrode fabricated by coating SiC nanowires with Pt nanoparticles has been specially designed to present high electrocatalytic activity and selectivity to study the sub-millisecond dynamics of the four primary reactive oxygen and nitrogen species (i.e., $ONOO^-$, H_2O_2, NO, and NO_2^-) produced within activated living macrophages. The fluxes of these reactive species could then be individually monitored during rapid homeostatic processes occurring in single activated phagolysosomes of murine RAW 264.7 macrophages.

The corresponding results established unambiguously that phagolysosomes mainly produce $ONOO^-$, NO and NO_2^- in approximately equal yields during continuous inflammatory situations. In comparison, only small amounts of H_2O_2 are produced contrary to general medical and biological beliefs. However, when a phagolysosome has to compensate for a sudden decrease in its internal ROS/RNS content, a complex homeostatic mechanism is triggered in an attempt to compensate for the ROS/RNS losses. Intense ROS/RNS bursts are then generated over a sub-millisecond time range, but with a radically different composition, mainly involving $ONOO^-$ and large excesses of NO.

These contrasting results revealed for the first time a drastic change in the relative activities of NOX (which mainly generate superoxide ions) and iNOS (which mainly generate nitric oxide) enzymatic pools when a phagolysosome switches from a continuous inflammatory state to a homeostatic one. Although unexpected, this drastic change in the relative activities of the enzymes appears to be the optimal solution for suddenly increasing pathogen clearance rates without overproducing destructive ROS/RNS that would endanger the phagolysosome and the macrophage itself.

Future developments of the electrochemical strategy presented in this work will undoubtedly provide a deep quantitative understanding of the complex mechanisms that allow phagocytosis. Due to the crucial importance of macrophages as a versatile first line of defense against diseases, bacteria, viruses, mutated cells, etc., we believe that the search for such detailed quantitative knowledge is fully justified.

ASSOCIATED CONTENT

Supporting Information

The Supporting Information is available free of charge at http://pubs.acs.org.

Experimental details and supplement data including characterization analysis, electrochemical measurements and cell experiments (PDF)

AUTHOR INFORMATION

Corresponding Author

Wei-Hua Huang-*College of Chemistry and Molecular Sciences, Wuhan University, Wuhan 430072, P. R. China; E-mail: whhuang@whu.edu.cn*

Christian Amatore-*State Key Laboratory of Physical Chemistry of Solid Surfaces, College of Chemistry and Chemical Engineering, Xiamen University, Xiamen 361005, P. R. China, and PASTEUR, Département de Chimie, École Normale Supérieure, PSL Research University, Sorbonne University, UPMC Univ. Paris 06, CNRS 24 rue Lhomond, Paris 75005, France; E-mail: christian.amatore@ens.psl.eu*

Authors

Yu-Ting Qi-*College of Chemistry and Molecular Sciences, Wuhan University, Wuhan 430072, P. R. China*

Hong Jiang-*College of Chemistry and Molecular Sciences, Wuhan University, Wuhan 430072, P. R. China*

Wen-Tao Wu-*College of Chemistry and Molecular Sciences, Wuhan University, Wuhan 430072, P. R. China*

Fu-Li Zhang-*College of Chemistry and Molecular Sciences, Wuhan University, Wuhan 430072, P. R. China*

Si-Yu Tian-*College of Chemistry and Molecular Sciences, Wuhan University, Wuhan 430072, P. R. China*

Wen-Ting Fan-*College of Chemistry and Molecular Sciences, Wuhan University, Wuhan 430072, P. R. China*

Yan-Ling Liu-*College of Chemistry and Molecular Sciences, Wuhan University, Wuhan 430072, P. R. China*

Complete contact information is available at: https://pubs.acs.org

Author Contributions

The manuscript was written through contributions of all authors. All authors have given approval to the final version of the manuscript.

Notes

The authors declare no competing financial interest.

ACKNOWLEDGMENT

We gratefully acknowledge financial support from the National Natural Science Foundation of China (Grants 21725504, 22090050, 22090051, and 21721005), the University of Xiamen and the State Key Laboratory of Physical Chemistry of Solid Surfaces (PCOSS, University of Xiamen, China) through a Distinguished Scientist Chair awarded to C.A. In France, it was supported in part by PSL University, École Normale Supérieure, CNRS, and Sorbonne University (UMR 8640). Both teams gratefully acknowledge the CNRS Sino-French support (LIA "Nano-BioCatEchem").

REFERENCES

(1) Vieira, O. V.; Botelho, R. J.; Grinstein, S., Phagosome maturation: aging gracefully. *Biochem. J.* **2002**, *366*, 689-704.
(2) Swanson, J. A., Shaping cups into phagosomes and macropinosomes. Nat. Rev. *Mol. Cell Biol.* **2008**, *9*, 639-649.
(3) Flannagan, R. S.; Cosío, G.; Grinstein, S., Antimicrobial mechanisms of phagocytes and bacterial evasion strategies. *Nat. Rev. Microbiol.* **2009**, *7*, 355-366.
(4) Russell, D. G.; VanderVen, B. C.; Glennie, S.; Mwandumba, H.; Heyderman, R. S., The macrophage marches on its phagosome: dynamic assays of phagosome function. *Nat. Rev. Immunol.* **2009**, *9*, 594-600.
(5) Weiss, G.; Schaible, U. E., Macrophage defense mechanisms against intracellular bacteria. *Immunol. Rev.* **2015**, *264*, 182-203.
(6) Gordon, S., Phagocytosis: an immunobiologic process. *Immunity* **2016**, *44*, 463-475.
(7) Nathan, C. F.; Hibbs, J. B., Role of nitric oxide synthesis in macrophage antimicrobial activity. *Curr. Opin. Immunol.* **1991**, *3*, 65-70.
(8) Bogdan, C.; Röllinghoff, M.; Diefenbach, A., Reactive oxygen and reactive nitrogen intermediates in innate and specific immunity. *Curr. Opin. Immunol.* **2000**, *12*, 64-76.
(9) Fang, F. C., Antimicrobial reactive oxygen and nitrogen species: concepts and controversies. *Nat. Rev. Microbiol.* **2004**, *2*, 820-832.
(10) Wang, Y.; Noel, J. M.; Velmurugan, J.; Nogala, W.; Mirkin, M. V.; Lu, C.; Collignon, M. G.; Lemaître, F.; Amatore, C., Nanoelectrodes for determination of reactive oxygen and nitrogen species inside murine macrophages. P*roc. Natl. Acad. Sci. U. S. A.* **2012**, *109*, 11534-11539.
(11) Amatore, C.; Arbault, S.; Guille, M.; Lemaître, F., Electrochemical monitoring of single cell secretion: vesicular exocytosis and oxidative stress. *Chem. Rev.* **2008**, *108*, 2585-2621.
(12) Hu, K.; Liu, Y. L.; Oleinick, A.; Mirkin, M. V.; Huang, W. H.; Amatore, C., Nanoelectrodes for intracellular measurements of reactive oxygen and nitrogen species in single living cells. *Curr. Opin. Electrochem.* **2020**, *22*, 44-50.
(13) Hu, K.; Li, Y.; Rotenberg, S. A.; Amatore, C.; Mirkin, M. V., Electrochemical measurements of reactive oxygen and nitrogen species inside single phagolysosomes of living macrophages. *J. Am. Chem. Soc.* **2019**, *141*, 4564-4568.
(14) Zhang, X. W.; Oleinick, A.; Jiang, H.; Liao, Q. L.; Qiu, Q. F.; Svir, I.; Liu, Y. L.; Amatore, C.; Huang, W. H., Electrochemical monitoring of ROS/RNS homeostasis within individual phagolysosomes inside single macrophages. *Angew. Chem., Int. Ed. Engl.* **2019**, *58*, 7753-7756.
(15) Clausmeyer, J.; Schuhmann, W., Nanoelectrodes: applications in electrocatalysis, single-cell analysis and high-resolution electrochemical imaging. *Trends Anal. Chem.* **2016**, *79*, 46-59.
(16) Ying, Y. L.; Ding, Z.; Zhan, D.; Long, Y. T., Advanced electroanalytical chemistry at nanoelectrodes. *Chem. Sci.* **2017**, *8*, 3338-3348.
(17) Zhang, X. W.; Qiu, Q. F.; Jiang, H.; Zhang, F. L.; Liu, Y. L.; Amatore, C.; Huang, W. H., Real-time intracellular measurements of ROS and RNS in living cells with single core-shell nanowire electrodes. *Angew. Chem., Int. Ed.* **2017**, *56*, 12997-13000.
(18) Zhang, J.; Zhou, J.; Pan, R.; Jiang, D.; Burgess, J. D.; Chen, H. Y., New frontiers and challenges for single-cell electrochemical analysis. *ACS Sens.* **2018**, *3*, 242-250.
(19) Lu, S. M.; Peng, Y. Y.; Ying, Y. L.; Long, Y. T., Electrochemical sensing at a confined space. *Anal. Chem.* **2020**, *92*, 5621-5644.
(20) Pan, C.; Wei, H.; Han, Z.; Wu, F.; Mao, L., Enzymatic electrochemical biosensors for in situ neurochemical measurement. *Curr. Opin. Electrochem.* **2020**, *19*, 162-167.
(21) Zhang, X.; Hatamie, A.; Ewing, A. G., Nanoelectrochemical analysis inside a single living cell. *Curr. Opin. Electrochem.* **2020**, *22*, 94-101.
(22) Taupin, C.; Dvolaitzky, M.; Sauterey, C., Osmotic pressure induced pores in phospholipid vesicles. *Proc. Natl. Acad. Sci. U. S. A.* **1974**, *72*, 348-352.
(23) Amatore, C.; Arbault, S.; Bouton, C.; Drapier, J. C.; Ghandour, H.; Koh, A. C., Real-time amperometric analysis of reactive oxygen and nitrogen species released by single immunostimulated macrophages. *ChemBioChem* **2008**, *9*, 1472-1480.
(24) Amatore, C.; Arbault, S.; Bruce, D.; de Oliveira, P.; Erard, M.; Vuillaume, M., Characterization of the electrochemical oxidation of peroxynitrite: relevance to oxidative stress bursts measured at the single cell level. *Chem. Eur. J.* **2001**, *7*, 4171-4179.
(25) Amatore, C.; Arbault, S.; Bouton, C.; Coffi, K.; Drapier, J. C.; Ghandour, H.; Tong, Y., Monitoring in real time with a microelectrode the release of reactive oxygen and nitrogen species by a single macrophage stimulated by its membrane mechanical depolarization. *ChemBioChem* **2006**, *7*, 653-661.

(26) Li, Y.; Sella, C.; Lemaître, F.; Guille-Collignon, M.; Thouin, L.; Amatore, C., Electrochemical Detection of nitric oxide and peroxynitrite anion in microchannels at highly sensitive platinum-black coated electrodes. application to Ros and Rns mixtures prior to biological investigations. *Electrochim. Acta* **2014**, *144*, 111-118.
(27) Pan, R.; Hu, K.; Jia, R.; Rotenberg, S. A.; Jiang, D.; Mirkin, M. V., Resistive-pulse sensing inside single living cells. *J. Am. Chem. Soc.* **2020**, *142*, 5778-5784.
(28) Li, X.; Majdi, S.; Dunevall, J.; Fathali, H.; Ewing, A. G., Quantitative measurement of transmitters in individual vesicles in the cytoplasm of single cells with nanotip electrodes. *Angew. Chem., Int. Ed.* **2015,** *54*, 11978-11982.
(29) Lovric, J.; Najafinobar, N.; Dunevall, J.; Majdi, S.; Svir, I.; Oleinick, A.; Amatore, C.; Ewing, A. G., On the mechanism of electrochemical vesicle cytometry: chromaffin cell vesicles and liposomes. *Faraday discuss.* **2016**, *193*, 65-79.
(30) Phan, N. T. N.; Li, X.; Ewing, A. G., Measuring synaptic vesicles using cellular electrochemistry and nanoscale molecular imaging. *Nat. Rev. Chem.* **2017**, *1*, 0048.
(31) Decoursey, T. E.; Ligeti, E., Regulation and termination of nadph oxidase activity. *Cell. Mol. Life Sci.* **2005**, *62*, 2173-2193.
(32) Winterbourn, C. C.; Kettle, A. J.; Hampton, M. B., Reactive oxygen species and neutrophil function. *Annu. Rev. Biochem.* **2016**, *85*, 765-792.
(33) Wink, D. A.; Hines, H. B.; Cheng, R. Y.; Switzer, C. H.; Flores-Santana, W.; Vitek, M. P.; Ridnour, L. A.; Colton, C. A., Nitric oxide and redox mechanisms in the immune response. *J. Leukocyte Biol.* **2011**, *89*, 873-891.
(34) Williams, E. H.; Davydov, A. V.; Motayed, A.; Sundaresan, S. G.; Bocchini, P.; Richter, L. J.; Stan, G.; Steffens, K.; Zangmeister, R.; Schreifels, J. A.; Rao, M. V., Immobilization of streptavidin on 4h–SiC for biosensor development. *Appl. Surf. Sci.* **2012**, *258*, 6056-6063.
(35) Zhang, Q.; Luo, Q.; Qin, Z.; Liu, L.; Wu, Z.; Shen, B.; Hu, W., Self-assembly of graphene-encapsulated Cu composites for nonenzymatic glucose sensing. *ACS Omega* **2018**, *3*, 3420-3428.
(36) Sun, S.; Yang, D.; Zhang, G.; Sacher, E.; Dodelet, J. P., Synthesis and Characterization of platinum nanowire-carbon nanotube heterostructures. *Chem. Mater.* **2007**, *19*, 6376-6378.
(37) Sun, S.; Yang, D.; Villers, D.; Zhang, G.; Sacher, E.; Dodelet, J. P., Template- and surfactant-free room temperature synthesis of self-assembled 3D Pt nanoflowers from single-crystal nanowires. *Adv. Mater.* **2008**, *20*, 571-574.
(38) Meng, H.; Xie, F.; Chen, J.; Sun, S.; Shen, P. K., Morphology controllable growth of pt nanoparticles/nanowires on carbon powders and its application as novel electro-catalyst for methanol oxidation. *Nanoscale* **2011**, *3*, 5041-5048.
(39) Meng, H.; Zhan, Y.; Zeng, D.; Zhang, X.; Zhang, G.; Jaouen, F., Factors influencing the growth of Pt nanowires via chemical self-assembly and their fuel cell performance. *Small* **2015**, *11*, 3377-3386.
(40) Fan, W. T.; Qin, Y.; Hu, X. B.; Yan, J.; Wu, W. T.; Liu, Y. L.; Huang, W. H., Stretchable electrode based on Au@Pt nanotube networks for real-time monitoring of ROS signaling in endothelial mechanotransduction. *Anal. Chem.* **2020**, *92*, 15639-15646.
(41) Chen, J.; Herricks, T.; Geissler, M.; Xia, Y., Single-crystal nanowires of platinum can be synthesized by controlling the reaction rate of a polyol process. *J. Am. Chem. Soc.* **2004**, *126*, 10854-10855.
(42) Lee, E. P.; Peng, Z.; Cate, D. M.; Yang, H.; Campbell, C. T.; Xia, Y., Growing Pt nanowires as a densely packed array on metal gauze. *J. Am. Chem. Soc.* **2007**, *129*,10634-10635.
(43) Hall, S. B.; Khudaish, E. A.; Hart, A. L., Electrochemical oxidation of hydrogen peroxide at platinum electrodes. Part 1. an adsorption-controlled mechanism. *Electrochim. Acta* **1998**, *43*, 579-588.
(44) Wu, W. T.; Jiang, H.; Qi, Y. T.; Fan, W. T.; Yan, J.; Liu, Y. L.; Huang, W. H., Large-scale synthesis of functionalized nanowires to construct nanoelectrodes for intracellular sensing. *Angew. Chem., Int. Ed.* **2021**, *60*, 19337-19343.
(45) Schroder, K.; Hertzog, P. J.; Ravasi, T.; Hume, D. A., Interferon-gamma: an overview of signals, mechanisms and functions. *J. Leukocyte Biol*. **2004**, 75, 163-189.
(46) Billiau, A.; Matthys, P., Interferon-gamma: a historical perspective. *Cytokine Growth Factor Rev.* **2009**, *20*, 97-113.
(47) Bryant, C. E.; Spring, D. R.; Gangloff, M.; Gay, N. J., The molecular basis of the host response to lipopolysaccharide. *Nat. Rev. Microbiol.* **2010**, *8*, 8-14.
(48) Orecchioni, M.; Ghosheh, Y.; Pramod, A. B.; Ley, K., Macrophage polarization: different gene signatures in M1(LPS+) *vs.* classically and M2(LPS-) *vs.* alternatively activated macrophages. *Front. Immunol.* **2019**, *10*, 1084-1097.
(49) Van den Bossche, J.; O'Neill, L. A.; Menon, D., Macrophage immunometabolism: where are we (going)? *Trends Immunol.* **2017**, *38*, 395-406.
(50) Murray, P. J., Macrophage polarization. *Annu. Rev. Physiol.* **2017**, *79*, 541-566.
(51) Wen, Y.; Huo, F.; Wang, J.; Yin, C., Multicolor fluorescence based on fret regulated by functional peptides to screen high metastatic potential cancer cells. *Anal. Chem.* **2019,** *91*, 15057-15063.
(52) Zhang, P.; Ma, L.; Yang, Z.; Li, H.; Gao, Z., 5,10,15,20-Tetrakis(4-sulfonatophenyl)porphyrinato iron(III) chloride (FeTPPS), a peroxynitrite decomposition catalyst, catalyzes protein tyrosine nitration in the presence of hydrogen peroxide and nitrite. *J. Inorg. Biochem.* **2018**, *183*, 9-17.
(53) Mander, P.; Brown, G. C., Activation of microglial NADPH oxidase is synergistic with glial iNOS expression in inducing neuronal death: a dual-key mechanism of inflammatory neurodegeneration. *J. Neuroinflammation* **2005**, *2*, 20-35.
(54) Ali, T. K.; Matragoon, S.; Pillai, B. A.; Liou, G. I.; El-Remessy, A. B., Peroxynitrite mediates retinal neurodegeneration by inhibiting nerve growth factor survival signaling in experimental and human diabetes. *Diabetes* **2008**, *57*, 889-898.
(55) Szabó, C.; Ischiropoulos, H.; Radi, R., Peroxynitrite: biochemistry, pathophysiology and development of therapeutics. *Nat. Rev. Drug discovery* **2007**, *6*, 662-680.
(56) Ferrer-Sueta, G.; Campolo, N.; Trujillo, M.; Bartesaghi, S.; Carballal, S.; Romero, N.; Alvarez, B.; Radi, R., Biochemistry of peroxynitrite and protein tyrosine nitration. *Chem. Rev.* **2018**, *118*, 1338-1408.
(57) Oleinick, A.; Svir, I.; Amatore, C., 'Full Fusion' is not ineluctable during vesicular exocytosis of neurotransmitters by endocrine cells. *Proc. R. Soc. A* **2017**, *473*, 20160684.
(58) Denicola, A.; Souza, J. M.; Radi, R.; Lissi, E., Nitric oxide diffusion in membranes determined by fluorescence quenching. Arch. *Biochem. Biophys.* **1996**, *328*, 208-212.
(59) Denicola, A.; Souza, J. M.; Radi, R., Diffusion of peroxynitrite across erythrocyte membranes. *Proc. Natl. Acad. Sci. U. S. A.* **1998**, *95*, 3566-3571.
(60) Möller, M. N.; Lancaster, J. R.; Denicola, A., Chapter 2 the interaction of reactive oxygen and nitrogen species with membranes. *In Free Radical Effects on Membranes* **2008**, *61*, 23-42.
(61) Giacovazzi, R.; Ciofini, I.; Rao, L.; Amatore, C.; Adamo, C., Copper-amyloid-β complex may catalyze peroxynitrite production in brain: evidence from molecular modeling. *Phys. Chem. Chem. Phys.* **2014**, *16*, 10169-10174.

Insert Table of Contents artwork here

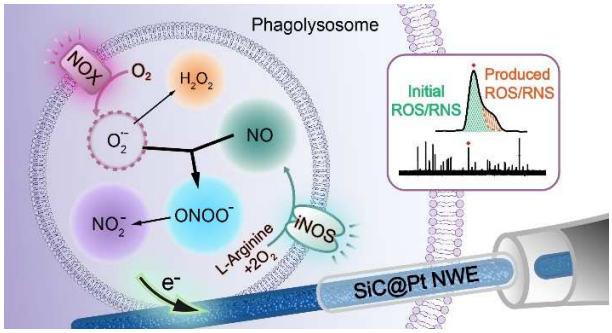

Homeostasis Inside Single Activated Phagolysosomes: Quantitative and Selective Measurements of Individual sub-Millisecond Dynamics of ROS/RNS Production with a Nanoelectrochemical Sensor

Supporting Information

Homeostasis Inside Single Activated Phagolysosomes: Quantitative and Selective Measurements of sub-Millisecond Dynamics of ROS/RNS Production with a Nanoelectrochemical Sensor

Yu-Ting Qi,[†] Hong Jiang,[†] Wen-Tao Wu,[†] Fu-Li Zhang,[†] Si-Yu Tian,[†] Wen-Ting Fan,[†] Yan-Ling Liu,[†] Christian Amatore,*[,‡,§] and Wei-Hua Huang*[,†]

[†] College of Chemistry and Molecular Sciences, Wuhan University, Wuhan 430072, P. R. China

[‡] State Key Laboratory of Physical Chemistry of Solid Surfaces, College of Chemistry and Chemical Engineering, Xiamen University, Xiamen 361005, P. R. China

[§] PASTEUR, Département de Chimie, École Normale Supérieure, PSL Research University, Sorbonne University, UPMC Univ. Paris 06, CNRS 24 rue Lhomond, Paris 75005, France

Table of Contents

- **Figure S11.** Voltammetric oxidation of (A) H_2O_2, (C) NO and (E) NO_2^- at different scan rates (V/s). Linear correlation of log peak current (lg i_p) *vs.* log scan rate (lg v) of (B) H_2O_2, (D) NO and (F) NO_2^-.
- **Figure S12.** Representative amperometric trace recorded at carbon layer modified SiC nanowire electrode (SiC@C NWE) at +850 mV inside IFN-γ/LPS stimulated RAW 264.7 macrophages.
- **Figure S13.** Representative amperometric traces recorded at +500 mV inside IFN-γ/LPS stimulated RAW 264.7 macrophages pre-incubated with (A) FeTPPS+CAT or (B) FeTPPS for 30 min.
- **Figure S14.** Bright-field and fluorescent images of IFN-γ/LPS stimulated RAW 264.7 macrophages with (right) and without (left) incubation with 1000 U/mL CAT for 30 min before staining with DCFH-DA.
- **Figure S15.** Representative amperometric traces recorded at +800 mV inside IFN-γ/LPS stimulated RAW 264.7 macrophages pre-incubated with (A) L-NMMA+apocynin or (B) 1400W+apocynin.
- **Figure S16.** Follow-up reactions of $O_2^{\cdot-}$ and NO yielding the four primary ROS/RNS.
- **Figure S17.** Bright-field and fluorescent images of M0 (left) or M1 (right) RAW 264.7 macrophages after staining with DAF-FM DA.
- **Figure S18.** Bright-field and fluorescent images of M0 (left) or M1 (right) RAW 264.7 macrophages after staining with DCFH-DA.

✧ **References**

Experimental Section

1. Materials and Instruments

SiC nanowires (SiC NWs) were bought from Nanjing/Jiangsu XFNANO Materials Tech Co., Ltd (Nanjing, China). Photoresist SU8-2002 was purchased MicroChem Corp (Newtown, U.S.A.). $H_2PtCl_6 \cdot 6H_2O$, peroxynitrite (sodium), lipopolysaccharide (LPS), catalase-polyethylene glycol (CAT, H_2O_2 scavenger), 5,10,15,20-tetrakis (4-sulfonatophenyl) porphyrinato iron (III) chloride (FeTPPS), apocynin, 1400W dihydrochloride , tetraacetoxymethylester (Calcein-AM), and propidium iodide (PI) were purchased from Sigma-Aldrich (St. Louis, U.S.A.). 3-aminoprooyltriethoxysilane (APTES) was bought from Aladdin Industrial Co., Ltd. (Shanghai, China). Formic acid was purchased from Chinasun Specialty Products Co., Ltd (Changshu, China). N^G-monomethyl-L-arginine monoacetate salt (L-NMMA), DAF-FM DA and DCFH-DA fluorescent probes were purchased from Beyotime Biotechnology Co., Ltd. (Shanghai, China). RAW 264.7 macrophages cell lines and cell culture medium were supplied by Procell Life Science & Technology Co., Ltd (Wuhan, China). Borosilicate capillary (1B100-4) was supplied by World Precision Instruments (U.S.A.). 80# Microcrystalline wax was purchased from Shuangfeng Wax Co., Ltd (Cangzhou, China) and was used to fabricate micropipette holders. All other chemicals and solvents of analytical grade were obtained from Sinopharm Chemical Reagent Co., Ltd. (Shanghai, China) and used as received unless stated otherwise. Ultrapure water (resistivity >18.2 MΩ·cm, Millipore Inc., U.S.A.) was used for rinsing and preparing all aqueous solutions.

Scanning electron microscopy (SEM) images were obtained with field-emission scanning electron microscopes (Zeiss Sigma and Zeiss Merlin Compact). Energy-dispersive X-ray spectroscopy (EDX) images were obtained with an EDX spectrometer (X-MaxN). Transmission electron microscopy (TEM) images were taken with a transmission electron microscope (JEM-2100). X-ray photoelectron spectroscopy (XPS) measurements were implemented on a photoelectron spectrometer (ESCALAB250Xi, Thermo Fisher Scientific). The C 1s peak (284.6 eV) was chosen as a reference to calibrate binding energies and Al Kα X-ray radiation was used as the X-ray source. Bright-field and fluorescent images were taken by an inverted fluorescent microscope (AxioObserver Z1 and Axiovert 200M, Zeiss). A microforge (World Precision Instruments, ×40 objective) was used to fabricate NWEs. Electrochemical measurements were conducted with a CHI 660e electrochemical workstation (CHI Instruments) in a two-electrode configuration with a homemade Ag/AgCl electrode of large size to perform simultaneously as a reference and a counter electrode. Amperometric recordings were achieved with a patch clamp amplifier (EPC-10, HEKA Electronics) coupled with a micromanipulator (TransferMan 4r, Eppendorf).

2. Modification of SiC NWs with APTES

SiC NWs (1 mg) were dispersed into ethanol (25 mL) via ultrasonication, before adding APTES (1

mL) in the suspension. Next, the mixture was ultrasonically treated, magnetically stirred, and maintained at 85 °C for 24 h. The resulting suspension was then washed 3 times with ethanol and ultrapure water respectively.

3. Synthesis of SiC@Pt NWs

We followed previously described guidelines reported in the literature,[1-5] after slightly modifying some steps as indicated below:

During the Pt-seeding reaction, SiC@APTES NWs were firstly dispersed into ultrapure water (15 mL) via ultrasonication, followed by 0.5 mM $H_2PtCl_6 \cdot 6H_2O$ and 0.3 M HCOOH addition into it. Next, the mixture was ultrasonically treated and kept steadily at 50 °C for 4 h until the solution turned black. Due to gravity, nanowires agglomerated at the bottom of reaction vessels. Finally, nanowires were collected and redispersed into ultrapure water again via ultrasonication.

During the second step, 0.5 mM $H_2PtCl_6 \cdot 6H_2O$ and 0.3 M HCOOH were added into the 15 mL dispersion of the freshly modified nanowires in ultrapure water, and the reaction temperature was adjusted to 25°C until the solution turned black completely (*ca.* for 2 h). SiC@Pt NWs were then collected at the bottom of the reaction vessel and washed 3 times with ultrapure water.

4. Fabrication of SiC@Pt NWEs

Mechanical procedures of NWEs fabrication were the same as in our previous works.[6,7] Prepared SiC@Pt NWs dispersed in 20 mL ultrapure water were added dropwise to the center of a glass sheet and gently heated to evaporate water. Then the glass sheet was cut into two parts to allow for a partial protrusion of NWs over glass slide edges. Next, using microforges manipulators, SiC@Pt NW was carefully inserted into a prepared glass micropipette holder filled with liquid metal and wax to fabricate a SiC@Pt NWE with the protruding length of SiC@Pt NW about 10 μm.

Subsequently, the SiC@Pt NWE was inserted into a glass capillary equipped with SU8-2002 for several seconds and quickly pulled out (Figure S7 step 1). This ensured that the protruding shaft of the SiC@Pt NWE was evenly coated with an insulating layer of SU8-2002.

Finally, a length of 2-3 μm at the tip of the insulated SiC@Pt NWE nanoelectrode was carefully inserted into a glass capillary filled with acetone for about 10 seconds to allow for a total SU8-2002 dissolution (Figure S7 step 2). The partially insulated nanoelectrodes were then stored at room temperature overnight to allow SU8-2002 to dry out completely.

5. Cell Experiment

5.1 Cells culture

RAW 264.7 cells were cultured in DMEM medium supplemented with 10% fetal bovine serum, 1% horse serum, and 1% penicillin-streptomyci at 37 °C under 5% CO_2 atmosphere. Before performing any experiment, the RAW 264.7 cells were seeded on small cell culture dishes (diameter 35 mm) in which 1 μg/mL LPS and 100 units/mL IFN-γ were simultaneously added. After incubation for 24 hours under cell culture conditions, the majority of M0 type macrophages were activated and transformed in M1 type.

5.2 Incubations of RAW 264.7 cells with ROS/RNS scavenger or enzyme inhibitor

IFN-γ/LPS stimulated RAW 264.7 were treated with 1000 U/mL CAT or 10 μM/L FeTPPS for 30 min before electrochemical detections.

500 μM/L apocynin, 1 mM/L L-NMMA or 10 μM/L 1400W were added with IFN-γ/LPS together to the cell medium for 24 h. Then the electrochemical detection was performed as soon as possible.

5.3 Fluorescence imaging of ROS/RNS in M0 and M1 RAW 264.7 macrophages

5.3.1 Cell viability experiment

SiC@Pt NWEs were inserted into RAW264.7 cells and then withdrawn, and the viability of penetrated cells was verified by fluorescence at once. The RAW264.7 cells were incubated with 1 mL fluorescence dye solution (Calcein-AM + PI) for 20 min, and residual dyes were washed off with PBS solution for 3 times. Bright-field and fluorescence microphotographs were then taken with an inverted fluorescent microscope as soon as possible.

5.3.2 Fluorescence imaging of ROS/RNS in RAW264.7 macrophages

M0 and M1 RAW 264.7 cells were incubated with 5 μM/L DAF-FM DA solution or 20 μM/L DCFH-DA for 25 min and washed 3 times with PBS. Bright-field and fluorescence microphotographs were then taken with an inverted fluorescent microscope as soon as possible.

6. Amperometric Data Acquisition and Analysis

All cell-free electrochemical experiments were performed using CHI 660e inside a well-grounded Faraday cage. Besides, all amperometric measurement involving living cells were performed inside a well-grounded Faraday cage under an inverted microscope control equipped with a 40× objective lens. Single SiC@Pt NWEs were inserted across cell membranes with a micromanipulator (TransferMan 4r, Eppendorf) under the microscope. The amperometric traces were recorded with a 2-electrode electrochemical system using a patch-clamp amplifier (EPC-10, HEKA Electronics, Germany) at different potentials *vs.* the Ag/AgCl electrode. Amperometric traces were sampled at 50 kHz and

Bessel-filtered at 2.9 kHz. The peak-to-peak noise value of platinized SiC@Pt NWEs before and after insertion was less than 5 pA (compare Figures S11 and S13).

Raw amperometric data were gathered with the “Pulse” software and analyzed by the “Igor Pro” software (Igor Pro, Wave Metrics) kindly provided by Dr. E. V. Mosharov from Columbia University.

The initial (Q_0) and produced (Q_{prod}) ROS/RNS contents of each recorded amperometric spike were obtained after separating mathematically the shoulder components from the normal IVIEC components using a homemade program implemented in Mathlab as previously described.[8,9]

Supporting Figures

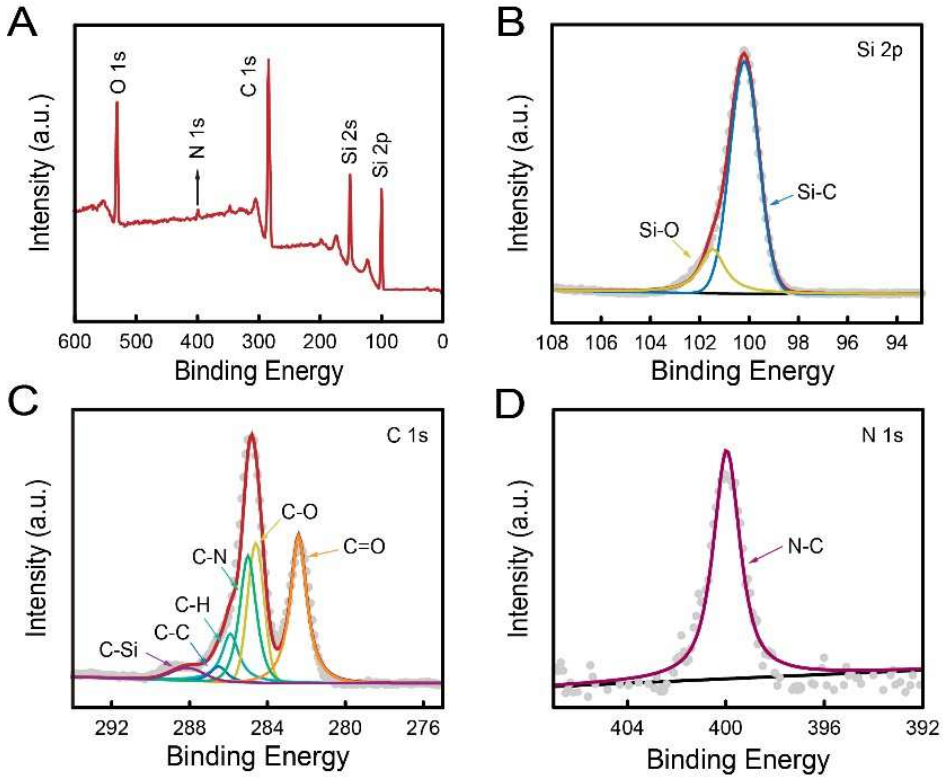

Figure S1. XPS spectra of SiC@APTES NWs. (A) complete XPS spectrum and detailed spectra of (B) Si 2p states, (C) C 1s states, and (D) N 1s states.

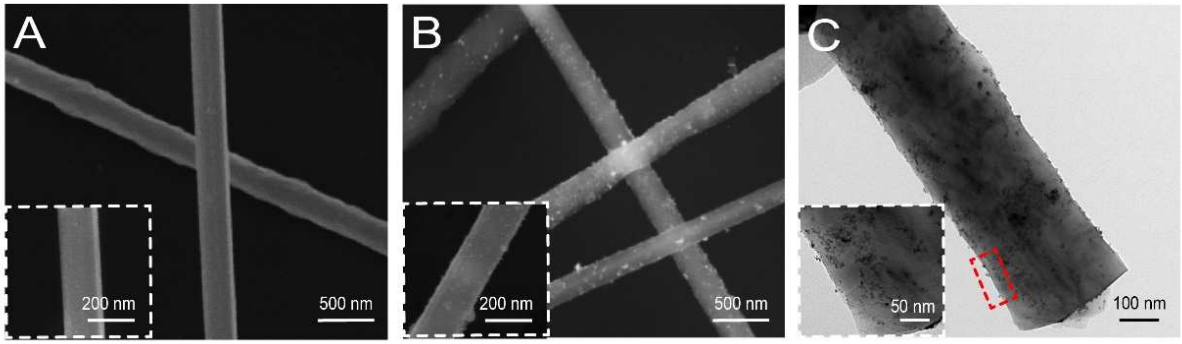

Figure S2. SEM images of (A) bare SiC NWs and (B) after initial Pt seeds deposition. (C) TEM images of SiC@Pt NWs after initial Pt seeds deposition. Insets: enlarged views.

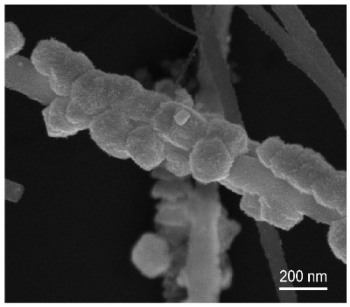

Figure S3. SEM image of SiC@Pt NWs obtained after adding excesses of HCOOH and H_2PtCl_6 without ultrasonic dispersion. [10,11]

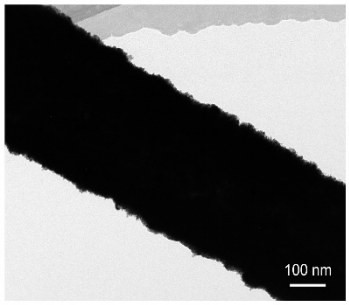

Figure S4. TEM image of a final SiC@Pt NW after second deposition stage.

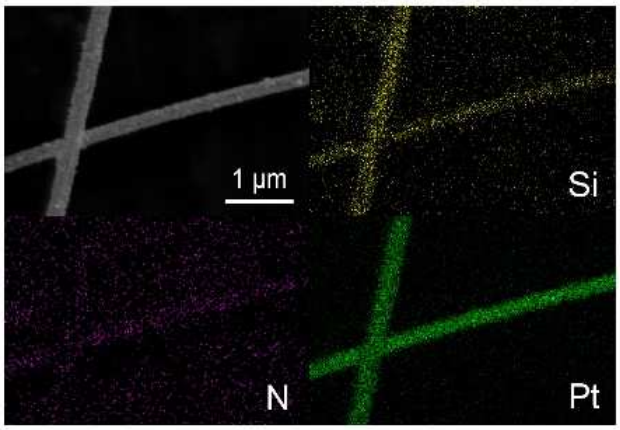

Figure S5. SEM image and EDX elemental mapping (N, Si, Pt) images of final SiC@Pt NWs.

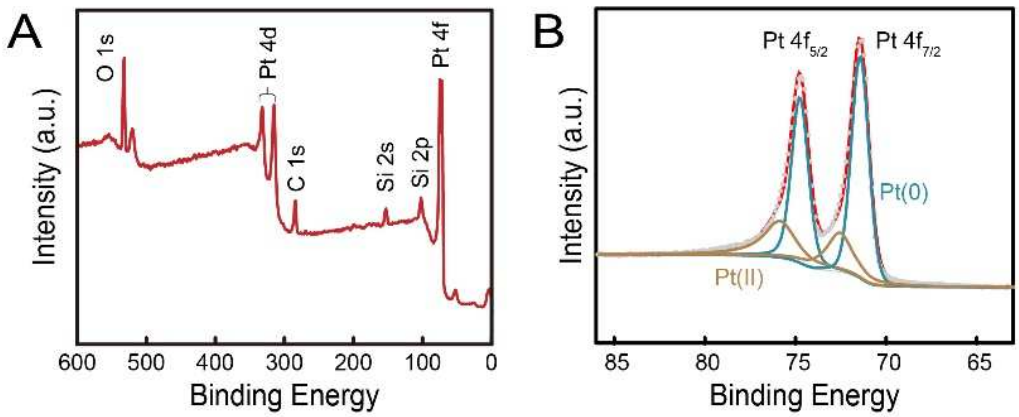

Figure S6. Figure S6. XPS spectra of final SiC@Pt NWs. (A) Complete spectrum and detailed spectra of (B) of Pt 4f states displaying the specific peaks at 71.4 eV (Pt $4f_{7/2}$) and 74.7 eV (Pt $4f_{5/2}$) attributable to Pt(0) state (cyan curves), and those at 72.5 eV (Pt $4f_{7/2}$) and 75.8 eV (Pt $4f_{5/2}$) featuring Pt(II) state (brown curves).

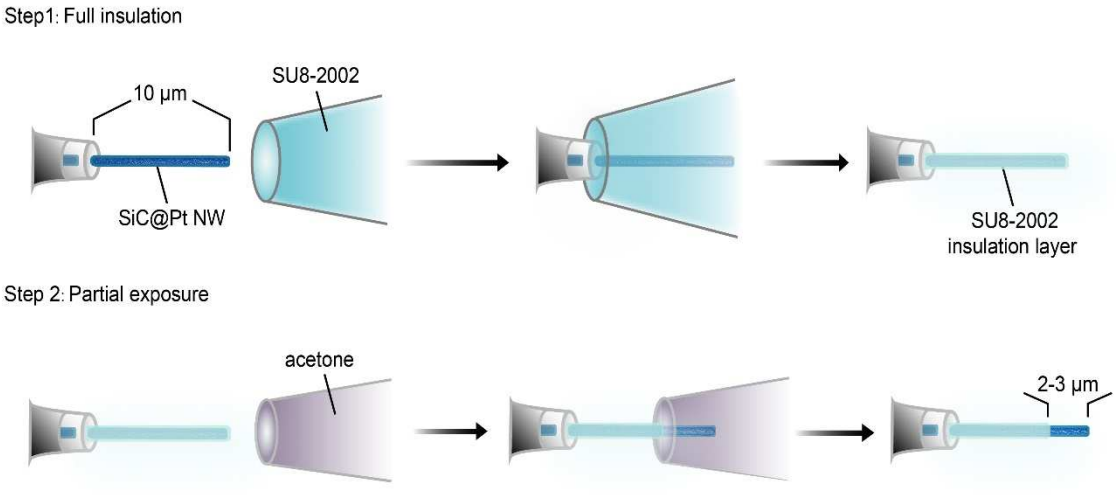

Figure S7. Schematic principle of insulating a mounted SiC@Pt NWE (step 1) and exposing its tip (step 2).

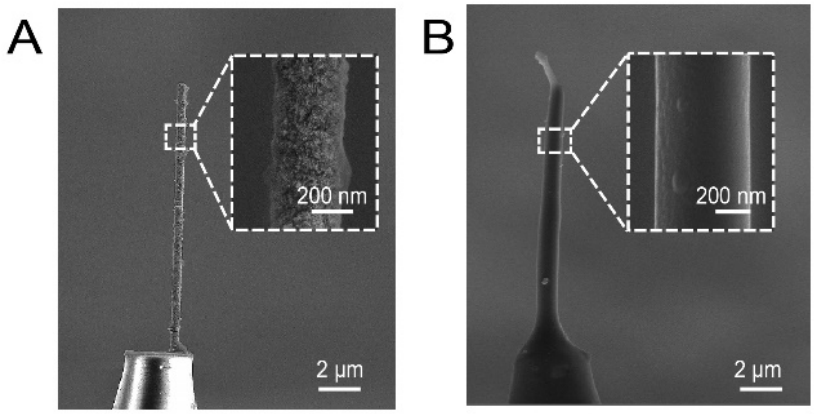

Figure S8. SEM images of a mounted SiC@Pt NWE (A) before its insulation and (B) after partial insulation of the exposed part with SU8-2002.

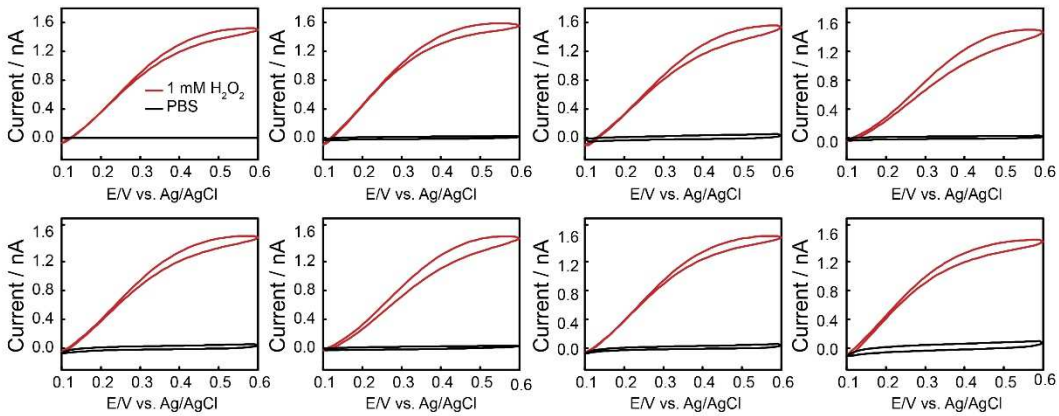

Figure S9. H_2O_2 anodic CVs recorded at 8 different SiC@Pt NWEs (H_2O_2, 1 mM in PBS). Baselines recorded in the absence of H_2O_2 are shown in black.

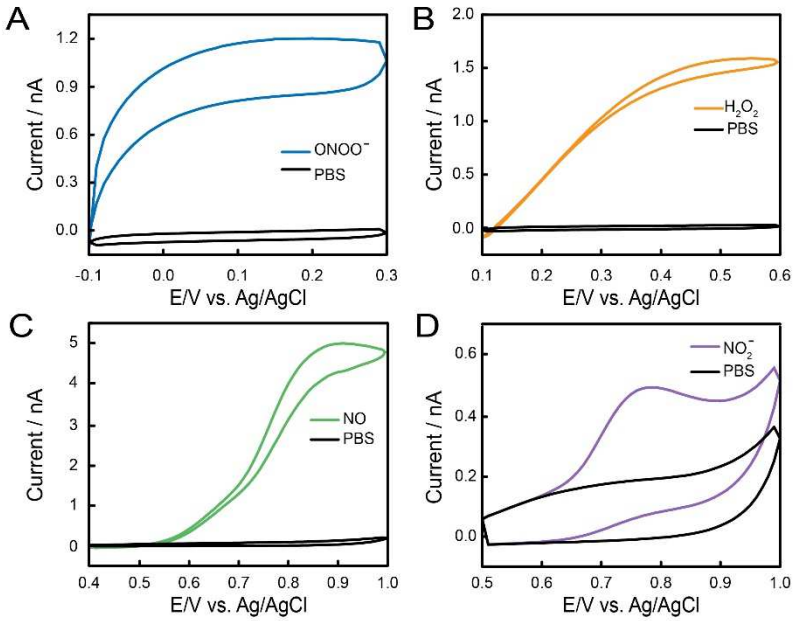

Figure S10. Anodic CVs of (A) $ONOO^-$ (pH=10.0, 1 mM),[12,13] (B) H_2O_2 (pH=7.4, 1 mM), (C) NO (pH=7.4, 1 mM)) and (D) NO_2^- (pH=7.4, 1 mM) in PBS, scan rate 0.1 V/s.

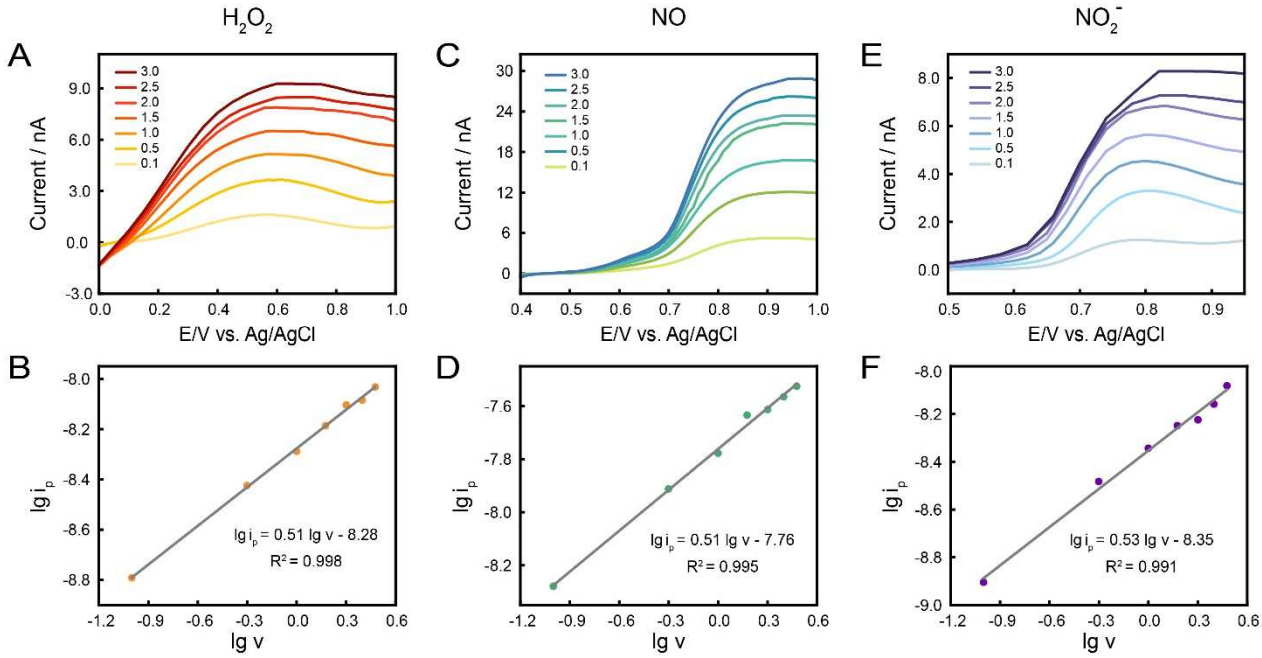

Figure S11. Voltammetric oxidation of (A) H_2O_2, (C) NO and (E) NO_2^- at different scan rate (V/s). Linear correlation of log peak current (lg i_p) *vs.* log scan rate (lg v) of (B) H_2O_2, (D) NO and (F) NO_2^- .

Figure S12. Representative amperometric trace recorded at carbon layer modified SiC nanowire electrode (SiC@C NWE) at +850 mV inside IFN-γ/LPS stimulated RAW 264.7 macrophages.

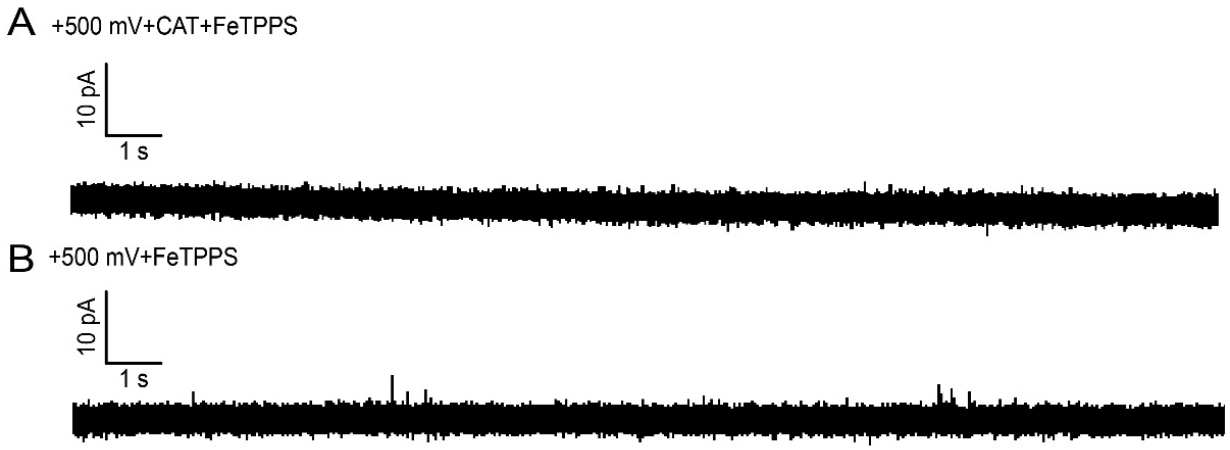

Figure S13. Representative amperometric traces recorded at +500 mV inside IFN-γ/LPS stimulated RAW 264.7 macrophages pre-incubated with (A) FeTPPS+CAT or (B) FeTPPS during for 30 min.

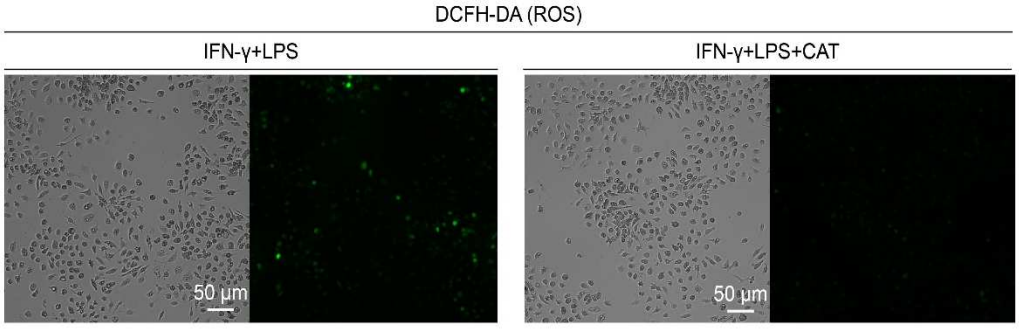

Figure S14. Bright-field and fluorescent images of IFN-γ/LPS stimulated RAW 264.7 macrophages with (right) and without (left) incubation with 1000 U/mL CAT for 30 min before staining with DCFH-DA.

Figure S15. Representative amperometric traces recorded at +800 mV inside IFN-γ/LPS stimulated RAW 264.7 macrophages pre-incubated with (A) L-NMMA+apocynin or (B) 1400W+apocynin.

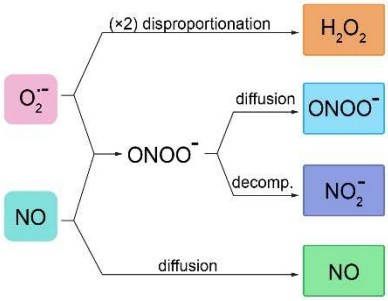

Figure S16. Follow-up reactions of $O_2^{\cdot-}$ and NO yielding the four primary ROS/RNS. More precisely, $O_2^{\cdot-}$ and NO, the precursors of all ROS/RNS, are generated by NOX and iNOS, respectively. $O_2^{\cdot-}$ disproportionates into H_2O_2 (stoichiometry: $2O_2^{\cdot-}$ per H_2O_2) either spontaneously or through catalysis by superoxide dismutase; $O_2^{\cdot-}$ also combines efficiently with NO to form $ONOO^-$ (stoichiometry: $1O_2^{\cdot-}$ and 1NO per $ONOO^-$) which is a transient species that rapidly evolves into its end-product NO_2^- (viz. corresponding also to $1O_2^{\cdot-}$ and 1NO per NO_2^-).[14,15] The residual NO excess is detected directly by diffusion to the nanoelectrode tip.

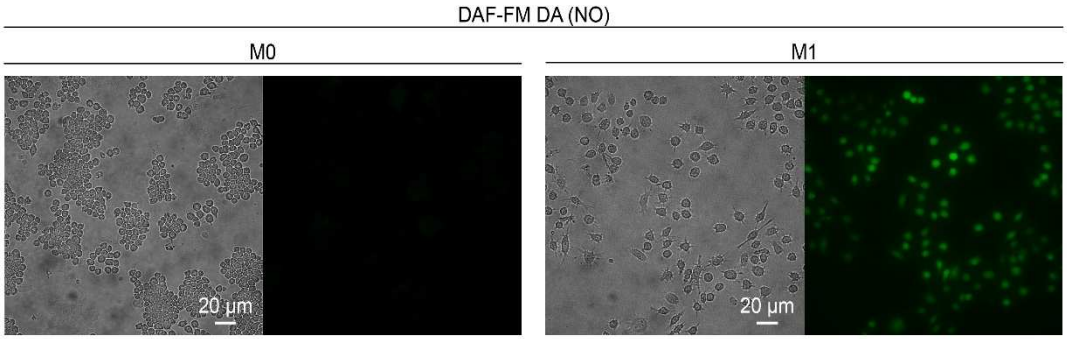

Figure S17. Bright-field and fluorescent images of M0 (left) or M1 (right) RAW 264.7 macrophages after staining with DAF-FM DA.

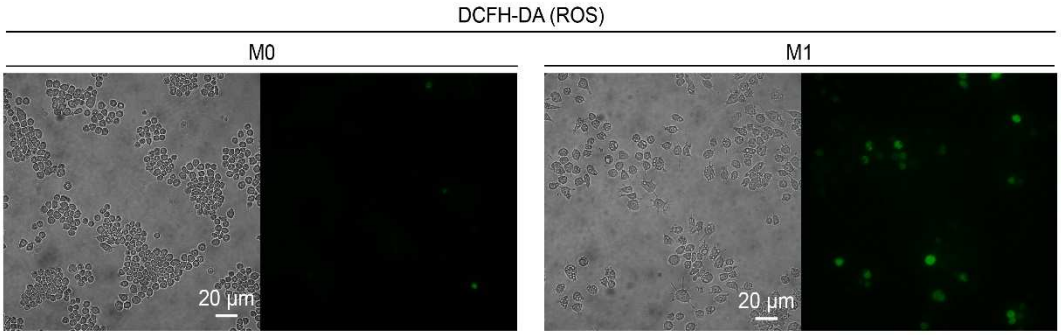

Figure S18. Bright-field and fluorescent images of M0 (left) or M1 (right) RAW 264.7 macrophages after staining with DCFH-DA.

REFERENCES

1. Sun, S.; Yang, D.; Zhang, G.; Sacher, E.; Dodelet, J. P., Synthesis and characterization of platinum nanowire-carbon nanotube heterostructures. *Chem. Mater.* **2007,** *19*, 6376-6378.
2. Sun, S.; Yang, D.; Villers, D.; Zhang, G.; Sacher, E.; Dodelet, J. P., Template- and surfactant-free room temperature synthesis of self-assembled 3d pt nanoflowers from single-crystal nanowires. *Adv. Mater.* **2008,** *20*, 571-574.
3. Meng, H.; Xie, F.; Chen, J.; Sun, S.; Shen, P. K., Morphology controllable growth of Pt nanoparticles/nanowires on carbon powders and its application as novel electro-catalyst for methanol oxidation. *Nanoscale* **2011,** *3*, 5041-5048.
4. Meng, H.; Zhan, Y.; Zeng, D.; Zhang, X.; Zhang, G.; Jaouen, F., Factors influencing the growth of Pt nanowires via chemical self-assembly and their fuel cell performance. *Small* **2015,** *11*, 3377-3386.
5. Fan, W. T.; Qin, Y.; Hu, X. B.; Yan, J.; Wu, W. T.; Liu, Y. L.; Huang, W. H., Stretchable electrode based on Au@Pt nanotube networks for real-time monitoring of ROS signaling in endothelial mechanotransduction. *Anal. Chem.* **2020,** *92*, 15639-15646.
6. Zhang, X. W.; Qiu, Q. F.; Jiang, H.; Zhang, F. L.; Liu, Y. L.; Amatore, C.; Huang, W. H., Real-time intracellular measurements of ROS and RNS in living cells with single core-shell nanowire electrodes. *Angew. Chem., Int. Ed.* **2017,** *56*, 12997-13000.
7. Wu, W. T.; Jiang, H.; Qi, Y. T.; Fan, W. T.; Yan, J.; Liu, Y. L.; Huang, W. H., Large-scale synthesis of functionalized nanowires to construct nanoelectrodes for intracellular sensing. *Angew. Chem., Int. Ed.* **2021,** *60*, 19337-19343.
8. Oleinick, A.; Svir, I.; Amatore, C., 'Full Fusion' is not ineluctable during vesicular exocytosis of neurotransmitters by endocrine cells. *Proc. R. Soc. A* **2017,** *473*, 20160684.
9. Zhang, X. W.; Oleinick, A.; Jiang, H.; Liao, Q. L.; Qiu, Q. F.; Svir, I.; Liu, Y. L.; Amatore, C.; Huang, W. H., Electrochemical monitoring of ROS/RNS homeostasis within individual phagolysosomes inside single macrophages. *Angew. Chem., Int. Ed.* **2019,** *58*, 7753-7756.
10. Chen, J.; Herricks, T.; Geissler, M.; Xia, Y., Single-crystal nanowires of platinum can be synthesized by controlling the reaction rate of a polyol process. *J. Am. Chem. Soc.* **2004,** *126* , 10854-10855.
11. Lee, E. P.; Peng, Z.; Cate, D. M.; Yang, H.; Campbell, C. T.; Xia, Y., Growing Pt nanowires as a densely packed array on metal gauze. *J. Am. Chem. Soc.* **2007,** *129*, 10634-10635.
12. Szabó, C.; Ischiropoulos, H.; Radi, R., Peroxynitrite: biochemistry, pathophysiology and development of therapeutics. *Nat. Rev. Drug Discovery* **2007,** *6*, 662-680.
13. Li, Y.; Sella, C.; Lemaître, F.; Guille-Collignon, M.; Thouin, L.; Amatore, C., Electrochemical detection of nitric oxide and peroxynitrite anion in microchannels at highly sensitive platinum-black coated electrodes. application to ROS and RNS mixtures prior to biological investigations. *Electrochim. Acta* **2014,** *144*, 111-118.

14. Amatore, C.; Arbault, S.; Bouton, C.; Coffi, K.; Drapier, J. C.; Ghandour, H.; Tong, Y., Monitoring in real time with a microelectrode the release of reactive oxygen and nitrogen species by a single macrophage stimulated by its membrane mechanical depolarization. *ChemBioChem* **2006,** *7*, 653-661.
15. Amatore, C.; Arbault, S.; Bouton, C.; Drapier, J. C.; Ghandour, H.; Koh, A. C., Real-time amperometric analysis of reactive oxygen and nitrogen species released by single immunostimulated macrophages. *ChemBioChem* **2008,** *9*, 1472-1480.